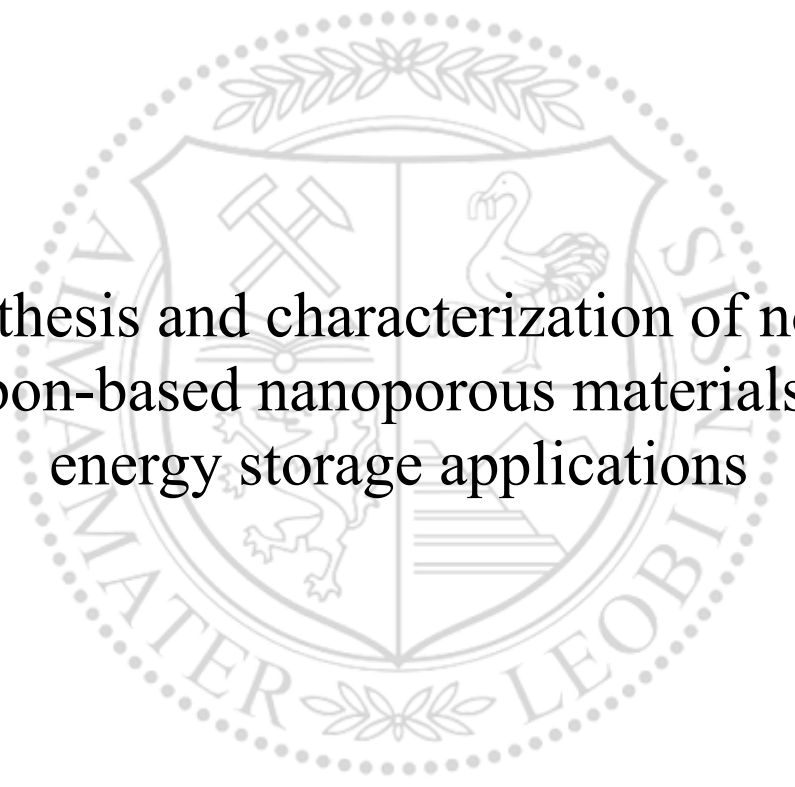Chair of Functional Materials and Materials Systems

Master's Thesis

Synthesis and characterization of novel carbon-based nanoporous materials for energy storage applications

Nikolas Rupert Natter, BSc

September 2020

EIDESSTATTLICHE ERKLÄRUNG

Ich erkläre an Eides statt, dass ich diese Arbeit selbständig verfasst, andere als die angegebenen Quellen und Hilfsmittel nicht benutzt, und mich auch sonst keiner unerlaubten Hilfsmittel bedient habe.

Ich erkläre, dass ich die Richtlinien des Senats der Montanuniversität Leoben zu "Gute wissenschaftliche Praxis" gelesen, verstanden und befolgt habe.

Weiters erkläre ich, dass die elektronische und gedruckte Version der eingereichten wissenschaftlichen Abschlussarbeit formal und inhaltlich identisch sind.

Datum 31.08.2020

Unterschrift Verfasser/in
Nikolas Rupert, Natter

Index of abbreviations

ACC	Activated carbon cloth
ACCcom	Commercially available activated carbon cloth
ACClab	Laboratory synthesized activated carbon cloth
APW	Average pore width
BET	Brunauer-Emmett-Teller
C	Capacitance
$C_{WE,s}$	Specific capacitance of the working electrode
CE	Counter electrode
CV	Cyclic voltammetry
CY	Ceramic yield
DFT	Density functional theory
DTA	Differential thermal analysis
E	Energy stored in a supercapacitor
EDLC	Electrical double-layer capacitor
EDX	Energy dispersive X-ray spectroscopy
EIS	Electrochemical impedance spectroscopy
ESR	Equivalent serial resistance
FTIR	Fourier-transform infrared radiation spectroscopy
hr	Hours
HTT1800	Durazane1800$^{®}$
m	Mass
m/z	Mass-to-charge ratio
min	Minutes
NLDFT	Non-local density functional theory
PDC	Polymer-derived ceramics
PSD	Pore size distribution
QSDFT	Quenched solid density functional theory
RE	Reference electrode
RMS	Root-mean-square
RT	Room temperature

S_{BET}	BET area
S_{DFT}	DFT area
SA	Surface area
SEM	Scanning electron microscopy
SSA	Specific surface area
TGA	Thermogravimetric analysis
TPV	Total pore volume
TPV_{DFT}	Total pore volume using the QSDFT method
$TPV_{Gurvich}$	Total pore volume using the single-point Gurvich rule
V	Voltage
WE	Working electrode
XRD	X-ray diffraction
Z'	Real part of impedance
Z"	Imaginary part of impedance
ϵ_0	Permittivity of vacuum
ϵ_r	Dielectric constant of the electrolyte
λ	Wavelength

Abstract

Rapid population growth and an increased desire for goods and comfort will lead to a strong increase of worlds energy consumption over the next decades. To overcome this challenge, existing energy systems need to become more efficient and new even more efficient technologies have to to be discovered. A very promising group of energy storage devices are supercapacitors due to their high energy output and long life-cycles. A supercapacitor consists of two electrodes that feature ultrahigh surface areas. The most common material for these applications is activated carbon. Recent studies emphasized the use of activated carbon cloth (ACC) that combines the advantages of activated carbon (e.g. high surface area) with the advantages of a cloth (i.e. flexibility and elasticity). Polymer-derived ceramics (PDCs) have been the subject of considerable research due to their performance properties such as extraordinary resistance towards oxidation and creep even at ultrahigh temperatures and their low energy consumption during synthesis. Depending on the chosen synthesis route, PDCs can show several other interesting characteristics such as catalytic or nanoporous properties. Therefore, by combining PDCs with ACC it could be possible to obtain nanocomposites (i.e. composites where at least one phase shows dimensions on the nanometric scale) that are very well suited for energy storage applications such as hydrogen storage or as electrodes in supercapacitors.

In this thesis, a laboratory synthesized ACC and a commercially available ACC have been impregnated with different PDCs. The PDCs consist of polysilazane that was mixed with different organometallics in toluene reflux in different ratios. Subsequent pyrolysis transformed the impregnated cloths into the final nanocomposites. Several characterization methods were used along the fabrication process to study the microstructural and morphological changes. Electrochemical studies were carried out to check the suitability of the created nanocomposites for energy storage applications. Porosity studies were performed to link the electrochemical performance to the porosity properties of the material.

It was found that the specific surface area as well as the total pore volume decreased compared to the pure ACC. This is attributed to potential pore blocking as a result of the impregnation process. The impregnation route also led to a very inhomogeneous impregnation. The electrochemical studies indicate that the produced nanocomposites are not suitable as electrodes for supercapacitors as a result of a decreased hysteresis loop (i.e. energy storage capability).

Kurzfassung

Rasantes Bevölkerungswachstum und ein verstärkter Wunsch nach Gütern und Komfort werden in den nächsten Jahrzehnten zu einem starken Anstieg des Weltenergieverbrauchs führen. Um diese Herausforderung zu bewältigen, müssen die bestehenden Energiesysteme effizienter genutzt werden, sowie noch effizientere Technologien entwickelt werden. Eine sehr vielversprechende Gruppe von Energiespeichermedien sind Superkondensatoren, aufgrund ihrer hohen Energieausbeute und langen Lebensdauer. Ein Superkondensator besteht aus zwei Elektroden, mit großen spezifischen Oberflächen. Das am häufigsten eingesetzte Material für Superkondensatorelektroden ist Aktivkohle. Studien betonen die Verwendung von äctivated carbon cloth"(ACC), das die Vorteile von Aktivkohle (z.B. große spezifische Oberfläche) mit den Vorteilen eines Tuches (d.h. Flexibilität und Elastizität) verbindet. "Polymer-derived ceramics"(PDCs) waren aufgrund ihrer Eigenschaften wie außerordentliche Oxidations- und Kriechbeständigkeit, auch bei ultrahohen Temperaturen, und ihres geringen Energieverbrauchs während der Synthese, Gegenstand beträchtlicher Forschungsarbeiten. Abhängig von der gewählten Syntheseroute können PDCs mehrere andere interessante Eigenschaften wie katalytische oder nanoporöse Eigenschaften aufweisen. Durch die Kombination von PDCs mit ACC könnten daher Nanoverbundwerkstoffe (d.h. Verbundwerkstoffe mit mindestens einer Phase mit Dimensionen im Nanometerbereich) erhalten werden, die sich sehr gut für Energiespeicheranwendungen wie Wasserstoffspeicherung oder als Elektroden in Superkondensatoren eignen könnten.

In dieser Arbeit wurden ein im Labor hergestellter ACC und ein kommerziell erhältlicher ACC mit verschiedenen PDCs imprägniert. Die PDCs bestehen aus Polysilazan, das mit verschiedenen Organometallverbindungen im Toluol-Reflux in unterschiedlichen Verhältnissen gemischt wurde. Durch anschließende Pyrolyse wurden die imprägnierten Tücher in die endgültigen Nanoverbundwerkstoffe umgewandelt. Entlang des Herstellungsprozesses wurden mehrere Charakterisierungsmethoden eingesetzt, um die mikrostrukturellen und morphologischen Veränderungen zu untersuchen. Elektrochemische Studien wurden durchgeführt, um die Eignung der hergestellten Nanoverbundwerkstoffe für Energiespeicheranwendungen zu überprüfen. Die Porositätseigenschaften der Materialen wurden ermittelt, um diese mit den elektrochemischen Eigenschaften des Materials in Verbindung zu bringen.

Es wurde festgestellt, dass sowohl die spezifische Oberfläche als auch das Gesamt-

porenvolumen im Vergleich zu reinen ACC abnahmen. Dies lässt sich auf eine mögliche Porenblockierung als Folge des Imprägnierungsprozesses zurückführen. Die gewählte Imprägnierungs-Route führte auch zu einer sehr inhomogenen Imprägnierung. Die elektrochemischen Untersuchungen deuten darauf hin, dass die hergestellten Nanoverbundwerkstoffe aufgrund einer verringerten Hystereseschleife (d.h. Energiespeicherfähigkeit) nicht als Elektroden für Superkondensatoren geeignet sind.

Key words

Activated carbon cloth

Characterization

Energy storage

Nanocomposites

Polymer-derived ceramics

Supercapacitor

Acknowledgements

Contents

1 Introduction

Over the past decades, a lot of research was focused on the development of nanocomposites in which the performance properties (e.g. mechanical, electrical, catalytical) can be designed according to the chosen synthesis route [1]. The designed properties of these nanocomposites can be significantly superior compared to the properties of conventional materials [2]. In nanocomposites, at least one phase shows dimensions on the nanometric scale [3]. A promising class of materials for nanocomposite purposes are so-called polymer-derived ceramics (PDCs), especially those based on silicon [4]. These materials enabled several significant breakthroughs such as ultrahigh temperature stable (i.e. up to 2000 °C) ceramic fibres and coatings. This is attributed to their extraordinary resistance towards oxidation and creep even at ultrahigh temperatures [5]. Another crucial advantage is the relatively low synthesis temperature compared to classical ceramics [5]. PDCs show great potential for catalytic applications as a result of the excellent controllability of the mesoporosity [6].

Rapid population growth and the increasing need for goods and comfort will lead to a severe ascent of global energy demand over the next decades [7, 8]. Therefore, an increasing use of renewable energy sources and the development of highly-efficient storage systems will be crucial to counter these obstacles [9, 10]. Battery systems are best suited for energy-intensive applications due to their high energy storage capacity [11]. Even though supercapacitors do not reach the energy densities of battery systems, their high energy output as well as their long life-cycles can be used as complimentary applications to battery systems, e.g. for electric vehicles [12]. A supercapacitor usually consists of two highly porous electrodes that are immersed in an electrolyte with a separator in between to avoid short circuits. The most common material for supercapacitor electrodes is activated carbon [11].

Activated carbon has been applied for highly-efficient water purification purposes for several decades [13, 14]. A more modern approach for the use of activated carbon is the storage of highly dense energy carriers such as hydrogen [15, 16]. A lot of research has also been devoted to the use of activated carbon in supercapacitor or battery devices, that could be an attractive alternative to the environmentally-harmful combustion of fossil fuels [16]. One very promising member of the group of activated carbons is the activated carbon cloth (ACC) due to its high specific surface area, adsorption capacity and mechanical

strength [17, 18]. Moreover, these materials combine the advantages of activated carbon (i.e. high specific surface area and specific pore volume) with the advantages of a cloth (i.e. flexibility and elasticity) [19].

The performance of carbon electrodes and therefore their adsorption and catalytic properties are strongly dependent on their surface morphology (e.g. pore structure) and on their surface chemistry (e.g functional groups) [20, 21]. The previously mentioned properties of PDCs such as controlled mesoporosity, low synthesis temperatures as well as their catalytic performance could be the key for energy storage applications. Thus, modifying the surface of a flexible and nanoporous ACC by using PDCs might yield potential for new high-efficient energy storage materials.

Therefore, several nanocomposites, using ACC and PDCs as precursors, were fabricated in this thesis. Two different ACC materials (i.e. laboratory fabricated ACC vs. commercially available ACC) were impregnated with different preceramic polymers. The PDCs produced in this thesis are based on polysilazane of the type HTT1800 mixed with nickel chlorine ($NiCl_2$) and cobalt chlorine ($CoCl_2$) in different ratios using a reaction at toluene reflux. The products of these reactions are called preceramic polymers, which were transformed into the final PDCs using pyrolysis at 700 °C in argon atmosphere. The nanocomposites were obtained via impregnation of the cloths with the different preceramic polymers that were dissolved in a certain amount of toluene. Subsequent drying of the impregnated materials and pyrolysis at 700 °C in argon atmosphere delivered the desired nanocomposites.

Several characterization techniques were used to study the microstructural and morphological changes as well as the surface chemistry properties along the fabrication process. By carrying out electrochemical measurements, the suitability of the nanocomposites for energy storage applications such as electrode material in supercapacitor applications was studied. N_2 gas ad-/desorption isotherms were measured to link the resulting electrochemical performance to its porosity properties.

2 Fundamentals

2.1 Supercapacitors

Supercapacitors, also called electrical double-layer capacitors (EDLC), are high power energy storage devices that were patented in 1957 and were commercially available for the first time in 1971 [11]. They consist of two electrodes with ultrahigh specific surface area (SSA) that are immersed in an electrolyte with a glass separator in between to avoid short circuits [22]. Even though supercapacitors do not reach the energy densities of modern battery systems, their long life-cycles and high power output (up to 10 kW kg^{-1}) make them an ideal compliment to battery systems for e.g. electric vehicles, where they are used during acceleration where a higher power output is needed [11]. The energy stored in a supercapacitor can be calculated using the following equation, where C is the capacitance and V is the voltage window [23].

$$E = \frac{C \cdot V^2}{2} \tag{2.1}$$

Consequently, a doubling of the applied voltage leads to an increase of stored energy by a factor of 4. Although increasing the voltage seems convenient, it could be shown that an operation voltage above 3 V has a negative impact on the high cycle life [24]. Furthermore, aqueous electrolytes start to decompose at even lower voltages, which further limits the maximum voltage window of supercapacitors that use aqueous electrolytes [25].

2.1.1 Charge storage

The basic principle of a supercapacitor is, that by applying a certain voltage, a highly reversible Helmholtz double-layer is formed at each electrode/electrolyte interface, which leads to the capacitance behaviour [10]. The main difference to batteries is that, in supercapacitors, the charge is stored on the surface rather than in bulk [11]. It is assumed that the capacitance of a supercapacitor can be calculated using the same formula as for a parallel-plate capacitor, where ϵ_r is the electrolyte dielectric constant, ϵ_0 is the permittivity of vacuum, SA is the surface area and d is the effective thickness of the electric double layer [26].

$$C = \frac{\epsilon_r \cdot \epsilon_0 \cdot SA}{d} \tag{2.2}$$

Consequently, by using two materials with a very high SA (i.e. SSA), capacitance values that are several orders of magnitude higher than for classical capacitors, are possible to fabricate. Even though the Helmholtz model gives a simple explanation regarding the formation of the double layer, it fails to predict the behaviour of real systems, where influences such as the choice of electrolyte, ion diffusion and dipole moments arise [11].
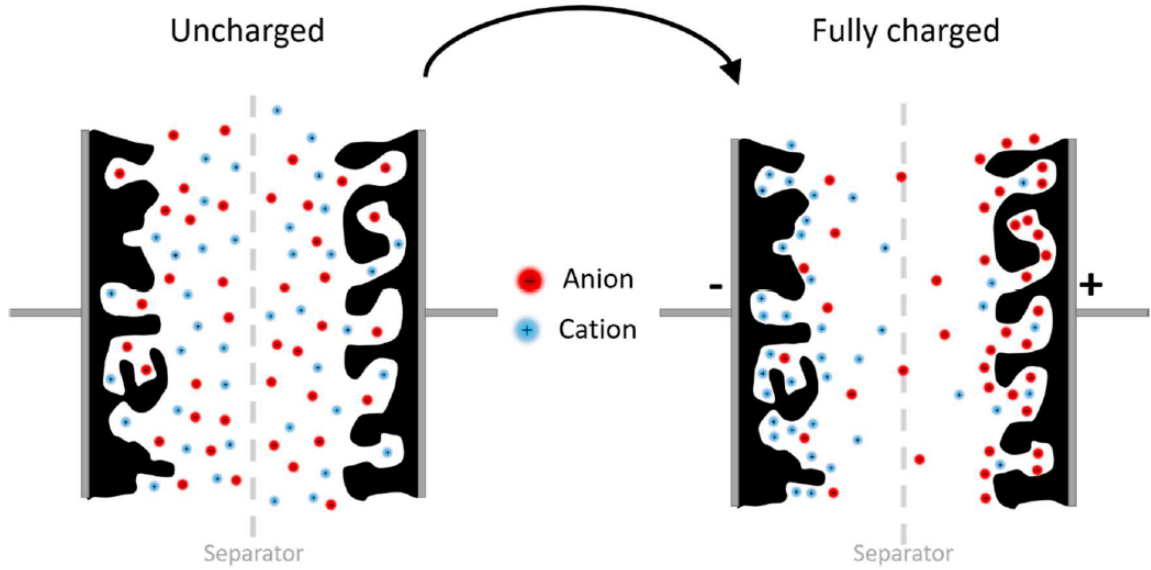

Fig. 2.1. Schematic representation of the formation of the Helmholtz double layer for porous carbons as illustrated by Koczwara [11].

2.1.2 Supercapacitor materials

The supercapacitor performance is strongly dependant on the SA of the electrode materials. However, not the entire SA of a supercapacitor material is accessible. Consequently, the measured capacitance values do not increase linearly with the SA [11]. Furthermore, the pore size and pore size distribution (PSD) of the electrodes have a major impact on the supercapacitor performance [27]. Largeot et al. found that, if the pore size is in the range of the ion size of the electrolyte, the capacitance reaches a maximum [28, 29]. Electrode materials can be divided into three main groups: carbon materials, conducting polymers and metal oxides [28]. Carbon materials are considered as the most promising materials for industrialisation as a result of properties such as abundance, easy processing, non-toxicity and high SSA [30]. On the other hand, the high resistivity, due to the contact resistance between carbon particles, gives rise to a high internal serial resistance, which limits the suitability of carbon materials as supercapacitor electrodes [30]. In general, activated carbon is the most common electrode material in supercapacitor applications, which is attributed to its good conductivity, long life-cycle and high accessible SA. [25].

Recent studies suggested the use of ACC as flexible and solid-state electrode materials (see section 2.2) [31–33].

2.1.3 Choice of electrolyte

As previously mentioned, the choice of the electrolyte can have a crucial influence on the supercapacitor performance (e.g. capacitance, maximum power output, etc.). Therefore, the electrolyte needs to feature several characteristics such as a wide voltage window, high electrochemical stability, low resistivity, low viscosity, low volatility, low toxicity, low cost as well as availability at high purity [28]. The commonly used electrolytes can be classified into the groups aqueous electrolytes, organic electrolytes and ionic liquids [11, 28].

2.1.4 Electrochemical measurements

Since it is not possible to reliably evaluate the performance of a supercapacitor only from structural properties such as SSA or PSD, a comprehensive electrochemical characterisation is necessary [34]. Typically the setup for electrochemical characterization can be divided into two main groups: two-electrode cell and three-electrode cell [11]. A two-electrode setup is used to evaluate the properties of real systems and consists of a working electrode (WE) and a counter electrode (CE) [11]. It can be set up symmetrically, where both electrodes have the same size, or asymmetrically, where one electrode is much larger than the other. An asymmetrical two-electrode setup is also referred to as half-cell setup [11]. The three-cell setup consists of the WE, the CE and a reference electrode (RE) [11]. A half-cell setup (i.e. asymmetric two-electrode setup) is used to evaluate the capacitance of only the WE. Therefore, a several times oversized CE has to be used. Some studies found that activated carbon can be used as a reliable quasi-reference for neutral aqueous electrolytes and ionic liquids [11, 35].

Cyclic voltammetry (CV) is a powerful tool to investigate the oxidation and reduction processes of molecular species and is based on the increase and decrease of current when a triangular voltage pattern is applied [36]. For a two-electrode setup with an oversized CE, the specific capacitance of the working electrode ($C_{\text{WE,s}}$) can be calculated according to

$$C_{\text{WE,s}} = \frac{\int_{t_0}^{t_1} I dt}{m \cdot \Delta U},$$ (2.3)

where I is the current, m is the mass of the WE and ΔU is the voltage window [35].

Electrochemical impedance spectroscopy (EIS) can be used to study several effects in supercapacitors such as pseudo-capacitance or ion diffusion [11]. One way of presenting EIS results are the so-called Nyquist plots, which illustrate the imaginary part of the impedance on the vertical axis and the real part of the impedance on the horizontal

axis [37]. The equivalent serial resistance (ESR) is another factor that limits the power and energy density of a supercapacitor [38]. No supercapacitor is perfect, and therefore all supercapacitors feature also non-capacitance behaviour, which can be described with the ESR [39]. It mainly depends on the diffusion layer thickness, which can be adjusted by external factors such as voltage, temperature and electrolyte concentration [39]. The ESR can be extracted graphically from a Nyquist plot as the point of intersection with the real axis, which corresponds to an infinite frequency [11].

2.2 Activated carbon cloth

Activated carbon cloth (ACC) usually gets fabricated via carbonization and activation of previously impregnated organic polymers such as viscose rayon cloth [40]. A major advantage of ACC is that it combines the properties of activated carbon such as high SA with the flexibility and elasticity of a cloth [19]. Furthermore, ACC features excellent adsorption capacity and mechanical strength [17,18]. Over the past decades, several studies dealt with the suitability of ACC in applications for environmental purposes such as adsorbents, electrodes or filters (e.g. waste water treatment from organic solvents or toxic pollutants) [41,42]. However, in recent years the focus of research shifted towards energy-related devices, where the cloths were tested as e.g. catalysts, electrodes or substrates [43]. Several of these studies revealed promising results of ACC towards three different applications, including H_2 storage, selective adsorption for the separation of CO_2/CH_4 mixtures and for energy storage applications such as electrodes in supercapacitors [17,31,32]. Furthermore, recent research revealed that the cloth-like nature of the ACC allows the fabrication of flexible and wearable supercapacitor devices [33,44]. Some studies also focused on the modification and impregnation of the ACC surface via e.g. an ammonia treatment to further improve its properties like capacitive deionization [45,46]. Some of these studies concluded that an impregnation of ACC with ammonia does not lead to subsequent pore blocking [47]. Furthermore, an impregnation procedure can also lead to the formation of additional pores on the ACC surface in the micro- and mesoporosity range [48].

2.3 Determination of porosity properties

Porosity properties are among the most crucial to evaluate the suitability of a material for energy storage applications [17]. Furthermore, the porosity properties of ACC also have a major impact on its suitability in many other applications such as H_2 storage or selective separation [17,19].

2.3.1   Specific surface area, pore size and pore shape

A very common characteristic used in surface-related reactions is the SA. This is attributed to the reliable indication that this parameter provides for the suitability of a material in surface-related reactions [13]. The SSA is defined as the SA over the total mass (m) of the sample [49]. The SSA is usually determined using gas ad-/desorption measurements (N_2, Ar or CO_2) and by using the Brunauer–Emmett–Teller (BET) method [49] or by applying the density functional theory (DFT) method [50]. Apart from the SSA, the pore shape, pore size and PSD are among the most important textural characteristics of porous materials [51–53].

According to the classification of the International Union of Pure and Applied Chemistry (IUPAC) [51], nanoporous materials can be classified according to their pore size into three main types:

- macropores: pores with widths exceeding 50 nm

- mesopores: pores with widths between 2 and 5 nm

- micropores: pores with widths smaller than 2 nm

In general, the term nanopore is defined by IUPAC as a pore with a width not exceeding 100 nm [51]. Micropores can be further distinguished into supermicropores with widths between 0.7 and 2 nm [54, 55] and ultramicropores with widths smaller than 0.7 nm [55].

The above-mentioned classification is mostly used for adsorption purposes [51]. As a result, the defined thresholds of each segment (i.e. macropores, mesopores etc.) are based on the different mechanisms that occur in the pores during N_2 ad-/desorption at 77 K and relative pressures up to 1. These are multilayer adsorption in macropores, capillary condensation in mesopores and micropore filling in micropores [51]. IUPAC uses the layer thickness of N_2 during an adsorption measurement as criteria to distinguish between micropores and ultramicropores. A N_2 layer is roughly 0.35 nm thick, as a result, the 0.7 nm limit corresponds to the thickness of a bilayer [51].

By assuming an infinitely extended slit-like pore, the average pore width (APW) can be estimated according to [17]

$$APW = \frac{2 \cdot TPV_{\text{DFT}}}{S_{\text{DFT}}},\qquad(2.4)$$

where TPV_{DFT} and S_{DFT} are the total pore volume (TPV) and the SSA of the material calculated using the DFT method.

Pores can also be distinguished based on their pore geometry. As shown in Fig. 2.2, pores can be divided into four different geometrical shapes: cylinder, slit-shape, cone-shape and ink-bottle according to Kaneko [52]. IUPAC uses a very similar classification with the only difference that they use a funnel-shape instead of a cone-shape [55]. For

simplicity reasons and because of the irregularity in geometry, it is often necessary to combine different forms of pore geometries to realistically model the porous characteristics of a material [55]. Therefore, knowledge about several criteria including pore size, pore geometry, connectivity and orientation is required to achieve a realistic porosity property model of a material [55].
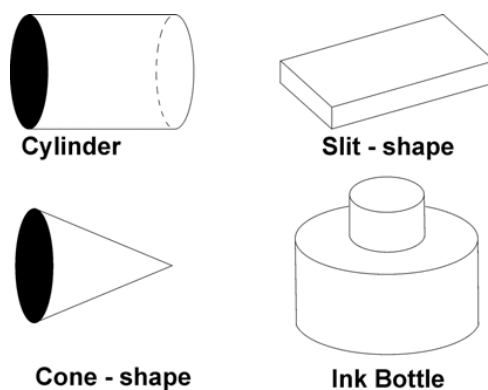

Fig. 2.2. Pore classification based on their geometry as proposed by Kaneko [52].

2.3.2 Ad-/desorption isotherms

According to IUPAC the ad-/desorption isotherms can be classified into six groups (I-VI) as summarized in Fig. 2.3. However, some isotherms are observed more frequently (i.e. type I, II and IV) than others (i.e. type III, V and VI) [56].

Type I isotherms are given for microporous solids that hardly have any external surfaces [51]. They can further be distinguished in type I(a) and type I(b). Type I(a) describes materials with mainly narrow micropores (below 1 nm) and a plateau in the isotherm at very low relative pressures [57]. Type I(b) refers to materials with a PSD over a broader range and wider micropores, which leads to a less steep increase and to a shorter plateau in the isotherm [51, 57]. The reversible type II isotherm is typical for non-porous or macroporous materials and results from unrestricted monolayer-multilayer adsorption up to high relative pressures as a result of macropores (> 50 nm) and/or external surface [51]. Type III is observed for nonporous materials with weak adsorbent-adsorbate interactions [58]. As a result, the adsorbed molecules are clustered around the most favourable sites, which leads to the absence of a monolayer [51]. Type IV refers to mesoporous materials and can further be subdivided into type IV(a) and type IV(b). While the non-reversible type IV(a) is observed for mesoporous materials that show capillary condensation which leads to the hysteresis loop between adsorption and desorption, type IV(b) refers to materials with only small mesopores [59]. A type V isotherm features weak adsorbent-adsorbate interactions accompanied by pore filling at higher relative pressures, which leads to a hysteresis loop [51]. Type VI is observed for materials that demonstrate layer-by-layer adsorption on highly uniform nonporous surfaces [51].
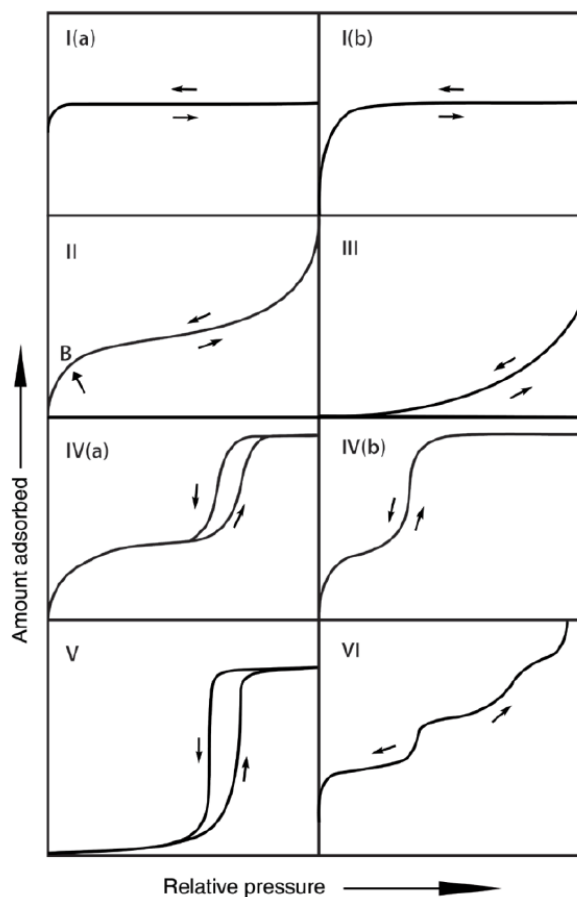
Fig. 2.3. IUPAC classification of the different types of isotherms [51].

2.3.3 Pore size distribution

The PSD is defined as the pore volume for each pore size and is plotted either as cumulative pore volume or as its derivative [60]. Usually, the PSD is measured using gas (N_2, Ar or CO_2) ad-/desorption isotherms at 77 K [43]. These isotherms can then be examined using two different theoretical approaches, i.e. molecular theory (microscopic approach) [59] or capillary condensation (macroscopic approach) [61]. One of the very common microscopic approaches is the non-local density functional theory (NLDFT), that describes the configuration of the adsorbed substances at a molecular level. Hence, factors like energetic and geometrical heterogeneities of an adsorbent material are taken into account [17]. An even better estimation for microporous materials yields the quenched solid density functional theory (QSDFT) that accounts for geometrical inhomogeneity [62]. However, the microscopic approach in general only delivers reliable results if the kernel (isotherms of different pore sizes with specific geometry corresponding to a determined interaction adsorbate–adsorbent) is suitably chosen [60].

2.4   Nanocomposites

A composite material is a material in which fibers or particles are embedded in a matrix of a different material, e.g. carbon fiber in a polymer matrix [63]. The composite exhibits new properties compared to the matrix alone, which allowed for several technological breakthroughs over the last decades, e.g. the invention of carbon-fiber reinforced plastics in aircrafts as light-weight, high-strength and high-rigid materials [64]. Apart from the composition, the materials can also differ in terms of size and shape (fibers, particles, etc.) of the fillers, which has an impact on properties like conductivity or reinforcement [64].

2.4.1   Definition of nanocomposites

Until the 1990s, almost only macrocomposites were fabricated with filler sizes in the micrometer range or larger [65]. Nanocomposites, in contrast to macrocomposites, consist of at least one Gibbsian solid phase (i.e. phases with specific, individual chemical composition and physical state), where at least one of the phases shows dimensions on the nanometric scale [3]. These nanometric phase(s) can be crystalline, semicrystalline or amorphous [3]. Even though carbon black was already used as a nanocomposite material in 1904, nanocomposites started to attract attention in the 1980s when the Toyota Motor Corporation started to use nylon-6 clay hybrid as engine timing belt covers [65,66]. The variety of used nanocomposite systems has been enlarged over the last decades and several systems based on metals, polymers and ceramics have been developed [1].

2.4.2   Polymer-derived ceramics

PDCs are a very promising group of materials for nanocomposite applications [67]. Although, these materials were fabricated for the first time back in the 1960s, the major hype in research activity did not come until the 1980s [68]. PDCs gained significant interest as a result of a variety of advantages during processing compared to classical ceramics. Apart from their excellent thermal, chemical and oxidation stability, the PDC route also features relatively low synthesis temperatures [5]. This leads to an economical and environmental benefit (i.e. less energy consumption) and also minimizes the alterations of other phases of the nanocomposites [5].

PDCs can easily be shaped into layers and fibers and they can also be modified to allow the formation of ordered pores [69,70]. Thus, it is possible to fabricate pores with sizes that range from nanometers to millimeters. Furthermore, a hierarchical porosity (micro-, meso- and macropores) can also be produced [71,72], which allows the controlling of the SSA according to the chosen synthesis parameters [72]. The catalytic performance of these materials can further be improved by anchoring or dispersing metals in the polymer matrix [6]. Moreover, other properties like e.g. the electrical conductivity and

creep resistance can be tailored by the choice of fillers and process parameters [5]. The PDC synthesis route is the only known way to fabricate complex systems based on Si-C-O, Si-C-N, Si-(E)-C-O and Si-(E)-C-N (where E is B, Al, Ti, etc.) ceramic systems [5].
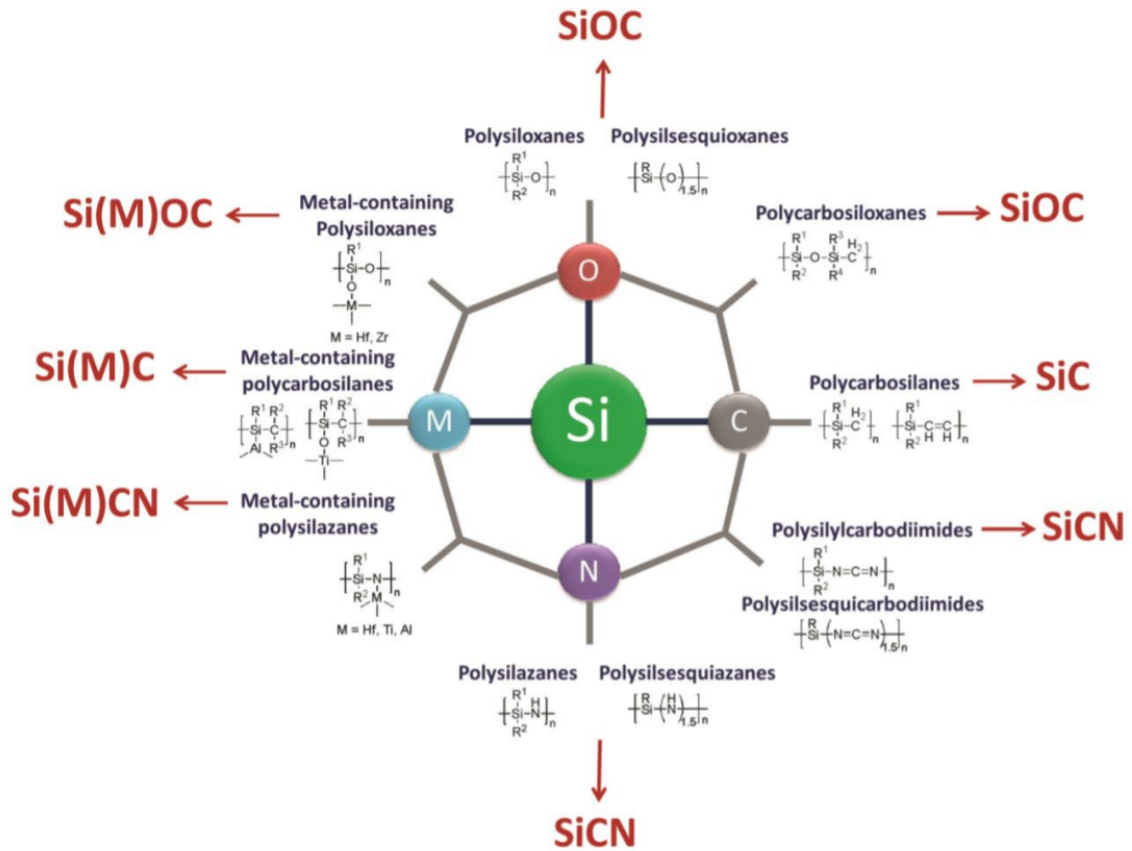

Fig. 2.4. Different groups of silicon-based polymer systems that can be used for PDCs as illustrated by Mera et al. [73].

Especially PDCs based on Si have gained significant interest over the last decades, as a lot of research was carried out to fabricate not only classical Si-based systems such as silicon carbide (SiC) or silicon nitride (Si_3N_4) but also to produce multinary component ceramics [69]. This is attributed to e.g. the ultrahigh temperature stability and high oxidation resistance of the quaternary Si-B-C-N system that was produced from poly-borosilazanes [70]. It could be found that the PDC route allows to easily control the phase composition and microstructure based on the chosen synthesis route and parameters [1,4]. Consequently, choosing the right preceramic polymers, with tailored molecular architecture, physico-chemical properties and suitable ceramization behavior is the crucial part to successfully fabricating PDCs [4]. Many properties of a PDC are governed by its amount of crystallinity. Thus, tailoring the synthesis parameters also allows to control the amounts of crystalline and amorphous parts in the sample [74].

Preceramic polymers should fulfill certain requirements to be suitable for PDC applications: (i) sufficiently high molecular weight to avoid volatilization; (ii) suitable rheological

properties; (iii) presence of reactive, functional group to allow cross-linking and (iv) the presence of rings or cages in the structure to hinder volatilization of the backbone [5].

The fabrication process of a PDC usually involves the steps shaping, crosslinking and conversion [6]. PDCs can be shaped using a wide range of different technologies such as tape casting, injection moulding or pressure-assisted sintering, just to name a few [5, 75]. The preceramic polymer, that is obtained from the crosslinking step, gets converted into a ceramic component through pyrolysis at a suitable temperature [5, 70].

As shown in Fig. 2.4, many different silicon-based systems exist to form different PDCs [73]. Among the most important are polysilanes, polycarbosilanes, polysiloxanes and polysilazanes that all feature different unique properties such as photo-conductivity, very high ceramic yields or good resistance against crystallization [5]. Polysilazanes, which are usually fabricated using an ammonolysis reaction of chlorosilanes with ammonia, have gained attention in recent years, due to their use as precursors for high-temperature stable SiCN ceramics [5, 76]. Other applications include the usage as precursors for SiCN and SiN_x dielectrics or as antigrafitty coatings [5, 77]. However, a major disadvantage is their sensitivity towards moisture and air [1].

Apart from the possibility to fabricate more complex systems and the low energy consumption, other useful advantages compared to classical synthesis routes arise. These include (i) pure starting compounds (precursors); (ii) no additives are necessary; (iii) the possibility to modify the molecular structure of the precursors; (iv) application of shaping technologies well known from plastic forming; (v) easy machining of the green body (i.e the shaped ceramic before sintering [78]) and (vi) the possibility to fabricate complex shapes that would not be possible with conventional methods [4, 5].

PDCs feature a broad range of different applications in key areas like information technology, transport and energy systems as a result of their functional properties and their versatile shapeability [5, 79]. Their use as fibers remains the most commercially successful application, however, PDCs also found use in other sophisticated technologies like micro- and nanoelectromechanical systems (MEMS/NEMS) or as biomedical components [80, 81].

3 Experimental methods

3.1 Materials

Two different ACC materials were used for impregnation. A laboratory synthesized version (hereafter denoted as ACClab) that was produced at the University of Belgrade in Serbia using carbonization and CO_2 activation of a viscose rayon cloth [17], as shown in Fig. 3.1. A commercially available ACC material (hereafter denoted as ACCcom) was provided by Evertech Envisafe Technology Co. Ltd. (Taiwan) and was used as a reference. The processing parameters of its fabrication are unknown, but the precursor was a viscose-based fiber material.
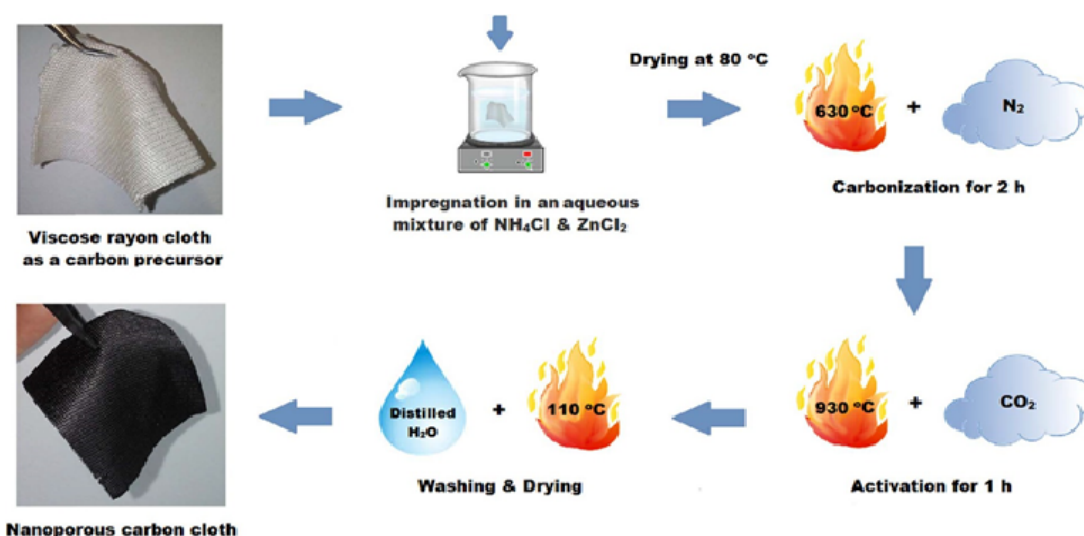
Fig. 3.1. Synthesis procedure of ACClab. The displayed temperatures correspond to the maximum values that were reached [17].

To make sure that the ACC samples did not contain any unwanted residues, the pure ACC samples were vacuum treated in a Carbolite GHA 12/450 furnace under vacuum (10^{-3} mbar) for 12 hr at 250 °C. To facilitate this procedure, the cloths of size $\sim$ 15 cm x 15 cm were cut into small strips of roughly 2 cm x 5 cm and stored in a glovebox before and after being vacuum treated.

The used preceramic polymers consist of different organometallics (i.e. chemical compounds that have at least one bond between a metal and a carbon atom of an organic

group [82]) mixed with a polysilazane of type Durazane® 1800 provided by Merck KGaA (hereafter denoted as HTT1800). Polysilazanes consist of alternate atoms of silicon and nitrogen as polymer backbone with methyl- and vinyl-groups as substituents [83, 84]. In this study, the organometallics cobalt(II) chloride ($CoCl_2$) provided by Merck KGaA and nickel(II) chloride ($NiCl_2$) provided by Aldrich, were used. The chemical structure of HTT1800 is shown in Fig. 3.2. HTT1800 was mixed with the organometallics in different ratios to form the desired preceramic polymers. 99.85% extra dry toluene provided by ACROS organics was used as solvent for the reaction.
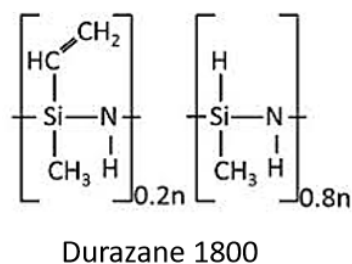

Fig. 3.2. Chemical structure of HTT1800 [83].

3.2 Synthesis of preceramic polymers

The preceramic polymers were created using a reaction of HTT1800 with different amounts of $NiCl_2$ and $CoCl_2$ in toluene at reflux (115 °C) in a three-necked round-bottom flask for 15 hr. All syntheses were carried out under argon atmosphere using standard Schlenk flask manipulations and vacuum/argon-line techniques. The Schlenk flasks were dried in an oven at 120 °C for 18 hr. All manipulations of the chemical components were carried out in a glovebox of type JAXOMEX GP (campus), where H_2O and O_2 concentrations were kept below 2 ppm. After putting the desired amount of organometallic in a three-necked round-bottom flask in the glovebox, the flask was sealed and mounted on a magnetic stirrer that was equipped with a heating plate. The flask was opened under argon flow to avoid any reaction with air. HTT1800 and toluene were added using passivated (i.e. flooded with argon) syringes before a water-cooled condenser was attached. The reaction was kept at room temperature (RT) for 3 hr before the temperature was gradually increased to 115 °C (i.e. boiling point of toluene) and kept at this value for 15 hr. The setup of the synthesis is shown in Fig. 3.3 as an example for a nickel (Ni) sample (Fig. 3.3a), before the condenser was attached, and for a cobalt (Co) sample (Fig. 3.3b), after the condenser was attached.

After 15 hr, the heating was switched off and the product was left to cool down naturally to RT before the condenser was detached. The solvent (i.e. toluene) was removed using a bridge and a solvent trap. In order to increase the efficiency of this process, the pressure was increased by covering the solvent trap in liquid N_2 and by

increasing the temperature of the three-necked round-bottom flask to 40 °C using the heating plate. After the extraction was completed, the flask was sealed and inserted into the glovebox where the synthesized preceramic polymer was collected. To avoid any subsequent contamination, the collector flask was sealed with parafilm.
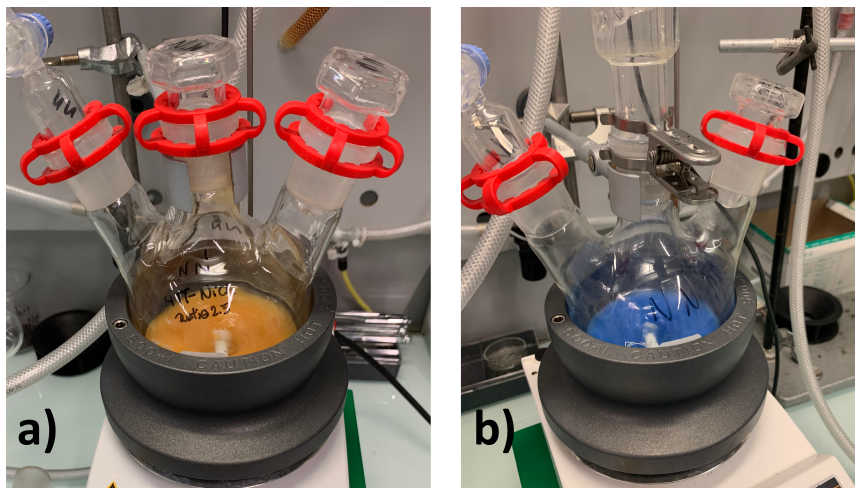

Fig. 3.3. a) Synthesis setup of the reaction of HTT1800 with $NiCl_2$ in toluene as solvent in a three-necked round-bottom flask mounted on a heating plate (before the condenser was attached). b) Synthesis setup of the reaction of HTT1800 with $CoCl_2$ in toluene as solvent in a three-necked round-bottom flask mounted on a heating plate and a magnetic stirrer (after the condenser was attached).

By using this method, 5 different samples were fabricated that feature different ratios of HTT1800 mixed with $CoCl_2$ and $NiCl_2$, respectively. The atomic ratio of silicon to metal equals the atomic ratio of HTT1800 to metal chloride):

- Si/Co = 2.5 (hereafter denoted as HTT-Co-2.5)

- Si/Co = 5 (hereafter denoted as HTT-Co-5)

- Si/Ni= 2.5 (hereafter denoted as HTT-Ni-2.5)

- Si/Ni = 5 (hereafter denoted as HTT-Ni-5)

- Si/Ni = 10 (hereafter denoted as HTT-Ni-10)

The reaction yield (i.e. the mass of the product divided by the mass of the precursors) was estimated for the HTT-Ni-10 to be 78%. It was assumed that this value is representative for all fabricated ratios and does also not change for Co.

3.3 Impregnation

The synthesis of the impregnation materials is similar to the synthesis of the pure preceramic polymers described in section 3.2. The difference from a process point of view

arises from the necessity of a liquid state impregnation material. Therefore, only a certain amount of toluene was extracted (i.e. after the extraction, the preceramic polymer is dissolved in a certain concentration of toluene). The desired mass ratio of preceramic polymer/ACC was set to be 1.4, because this value showed promising results in previous experiments. The concentration of preceramic polymer in toluene was kept at roughly 0.3 g/ml for all ratios. Therefore, the sum of the masses of HTT1800 and organometallic (before reaction) multiplied with the reaction yield (i.e. 78%) gives the amount of toluene that needs to be extracted.
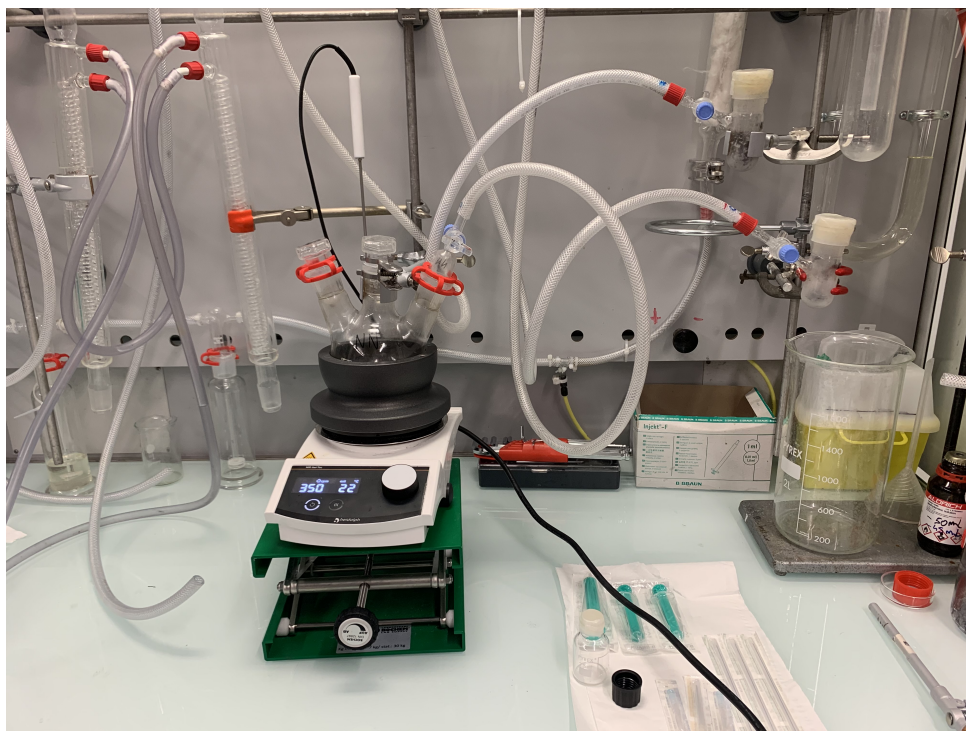

Fig. 3.4. Setup of the impregnation procedure with two small flasks on the right (one for ACClab, one for ACCcom) that are connected to the vacuum/argon-lines. On the left is the three-necked round-bottom Schlenk flask, where the impregnation material is kept under inert atmosphere.

To improve the impregnation process, the ACC materials were cut in even smaller pieces of ∼ 0.5 cm x 1 cm and placed in small flasks that were sealed with polymer membranes, as shown in Fig. 3.4. To avoid any contamination, this manipulation was carried out in a glovebox. The flasks were then connected to the argon/vacuum-tube system and static vacuum was set up in the flasks. After extracting the desired amount of toluene, the three-necked round-bottom flask was opened under argon flow and the impregnation material was taken using a passivated syringe. The needle of the syringe was then penetrating the membranes of the small flasks and the static vacuum within the small flasks sucked the impregnation material in. During impregnation, the syringes where rotated slightly to make the impregnation as evenly distributed along the cloth stripes, as possible. After the procedure, the small flasks were sealed with parafilm and

detached from the vacuum/argon-system. They were then placed in an ultrasonic bath for several hours. To wash the samples, toluene was added using a syringe. The toluene was extracted right after washing by using the same syringe. The samples were dried by applying a dynamic vacuum for 30 min before they were collected and subsequently stored in a glovebox.

3.4 Pyrolysis

The PDCs and the impregnated samples were pyrolyzed with the same heating program. All samples were placed in alumina crucibles and the polymer-to-ceramic conversions were performed in furnaces of type ThermoConcept ROS 50/450/12 and Carbolite GHA 12/450 from RT up to 700 °C with a heating rate of 5 °/min, 2 hr of holding time, under argon. The samples were left in the furnace to cool down naturally and were removed when RT was reached. Even though the obtained PDCs and nanocomposites should be non-reactive in air, all samples were stored in a glovebox after pyrolysis to avoid contamination.

3.5 Characterization

Due to the sensitivity of the polymers and precursors towards oxygen and moisture, the preceramic polymers required to be prepared in a glovebox for characterization studies. Thermogravimetric analysis (TGA) is a reliable tool to measure the ceramic yield (CY), which is the ratio of the mass of the transformed ceramic divided by the mass of the precursor material (i.e. preceramic polymer) [85]. Combined with mass spectrometry it enables to determine which gaseous substances formed during the polymer-to-ceramic conversion. The measurement also gives an indication at what temperature the conversion is finished. Thus, the minimum required temperature for the pyrolysis can be estimated. By combining these materials with a nanoporous material such as ACC, as done in this study, the conversion temperature has an even higher impact. The reason for this is that the pyrolysis temperature should be sufficient to convert the whole precursor into a ceramic but as low as possible to keep the nanoporous structure of the ACC materials as intact as possible. Differential thermal analysis (DTA) was performed to further investigate the thermal behaviour of the samples. TGA and DTA were carried out using a NETSCH STA 449 from RT up to 1000 °C at 5 °/min in argon atmosphere by using silica crucibles (sample mass $\sim$ 40 mg). An OmniStar cpp-295 was used for mass spectrometry in a temperature range from 200 °C up to 1000 °C. Mass spectrometry was only carried out for the ratio 5 samples of Co and Ni due to the assumption that the species that evolve during the conversion do not change for different ratios.

To analyze the bonding of the preceramic polymers, Fourier-transform infrared radiation spectroscopy (FTIR) was used. The polymers were measured by placing them

between KBr pellets (dried at 120 °C) in the case of liquid state polymers or by being embedded in a KBr matrix (in the case of clay/solid state polymers) and subsequent pressing into a pellet. FTIR was done using a ThermoScientific Nicolet 6700. Once more only the ratio 5 samples were measured, since it was assumed that the bonding structure should hardly be affected by the chosen ratio.

X-ray diffraction (XRD) was carried out using a BRUKER D8 Advance diffractometer measuring from $2\theta = 10°$ - 90° with a step size of 0.02°, step time of 0.85 s step^{-1} and $Cu_{K\alpha}$ ($\lambda = 1.54$ Å) radiation. All materials were grinded into fine powders to achieve better statistics.

To better understand the bonding of the final nanocomposites and of the pure ACC materials, Raman spectra were recorded using a Jobin-Yvon LABRAM confocal spectrometer equipped with a frequency-doubled Nd-YAG laser emitting at 532.2 nm. The laser beam was focused onto the sample by an Olympus BX 40 microscope fitted with a $\times50$ long-working distance objective lens at a power density of 0.1 mW/μm^2 and a spatial resolution of 1.5 cm^{-1}.

Surface morphology studies were done via scanning electron microscopy (SEM) measurements working at 10 kV and secondary electron topography. A JEOL JSM-IT-300LV was used for SEM that was combined with an Oxford Instruments X-MaxN to obtain energy dispersive X-ray (EDX) spectra. The average composition was calculated by averaging the composition values of several sections of the sample surface.

The fabricated nanocomposites and pure ACC samples were vacuum treated at 200 °C for 24 hours at 10^{-6} mbar in a Büchli B-580 oven, before they were characterized using XRD, gas ad-/desorption and electrochemical measurements to get rid of any unwanted residues of the impregnation process (e.g. Toluene), transport and storage.

The porosity properties of the samples were studied using a Quantachrome Autosorb iQ3 gas sorption analyzer from relative pressures of 10^{-6} using N_2 as adsorbate at 77 K. The samples were degassed for 24 hr under vacuum (10^{-6} mbar) at 200 °C. A filling rod was inserted into the sample cells to achieve more accurate and faster results. The measurements were only performed with the ACClab-based nanocomposites as well as pure ACClab. The ACCcom-based nanocomposites as well as pure ACCcom were not studied, since it was assumed that the impregnation procedure led to similar changes of the surface morphology for both ACC sample types. The SSA was calculated using the multi-point BET method (hereafter denoted as S_{BET}), following the BET consistency criteria of the International Standard Organization (ISO 9277:2010) and by applying the QSDFT method (hereafter denoted as S_{DFT}). However, BET is usually applied to mesoporous and macroporous materials and only approximates the SSA of microporous and ultramicroporous materials upon following specific criteria [86]. The PSD was estimated using the QSDFT method, where the N_2-carbon equilibrium transition kernel at 77.4 K for slit pores was used for all calculations. The TPV of the samples was calculated using

two different methods. The single-point Gurvich rule was applied for pores smaller than ~ 55 nm at relative pressures of 0.96. The method estimates the TPV by assuming that the pores are filled with liquid N_2 at relative pressures close to unity [56, 61]. The TPV was also calculated using the QSDFT method, even though the results are only reliable if the kernels are chosen correctly [60].

Electrochemical characterization studies were carried out by applying a Gamry Reference 600 potentiostat using a custom-built cell with a polyether ether ketone (PEEK) housing and Ti pistons that are connected to two separate electrical contacts. To achieve a constant pressure on the actual supercapacitor cell, the pistons were spring loaded. A half-cell setup was used with an approximately 8-times oversized counter electrode (CE) as quasi-reference for all measurements [87], as shown in Fig. 3.5a by Koczwara [11]. The CE consists of commercially available activated carbon YP-80F mixed with 5 wt.% polytetrafluorethylene (PTFE) binder in distilled water. The obtained paste was subsequently rolled in a rolling press until the CE had a thickness of ~ 300 μm and was then dried for 24 h at 120 °C at 5 mbar in a vacuum oven. The cells were built as a multi-layered assembly with two Pt current collectors, a CE of 12 mm diameter, a WE of 3 mm diameter and a glass fiber separator (Whatman GF/A) in between the electrodes. Aqueous 1 M caesium chloride (CsCl) solution was used as electrolyte. The WE was directly punched out of the nanocomposite using a die with a diameter of 3 mm. Since the ACCcom-based samples fell apart because of their poor structural integrity, compared to ACClab, while trying to punch out electrodes, the electrochemical measurements were only performed with the ACClab-based samples.
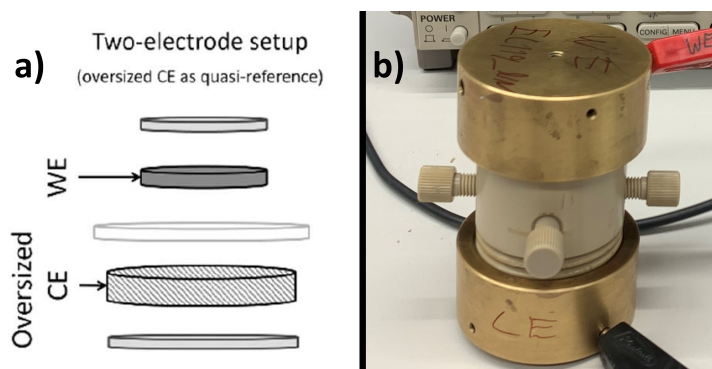

Fig. 3.5. a) Schematic representation of the half-cell setup with an oversized CE as quasi-reference, as shown by Koczwara [11]. b) photograph of the half-cell setup.

Cyclic voltammetry (CV) studies were done in a range of $\pm$ 0.6 V against the quasi-reference. CV curves were recorded for various scan rates ranging from 0.1 up to 1000 mV/s. The specific capacitance was calculated according to Eq. 2.3. Electrochemical impedance spectroscopy (EIS) measurements were carried out at 0 V with a root-mean-square (RMS) value of $\pm$ 5 mV over a frequency range from 10 mHz to 100 kHz with 10 points per decade.

4 Results and Discussion

4.1 Characterization of pristine ACC materials

To check the thermal stability of the already degassed ACC materials, TGA measurements were performed. In Fig. 4.1, TGA as well as their associate DTA curves are shown. By considering that DTA provides only qualitative information, it can be concluded that ACClab and ACCcom behave similarly and experience a weight loss of roughly 17.5% when exposed to temperatures of up to 1000 °C.
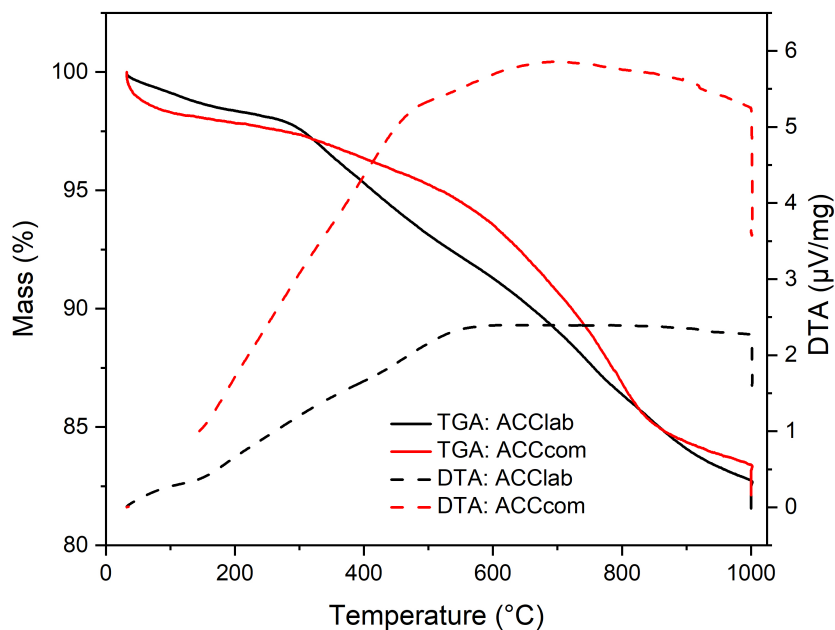
Fig. 4.1. TGA and DTA data of ACClab and ACCcom obtained between room temperature and 1000 °C under argon with a heating rate of 5 °C/min.

The X-ray diffractograms of ACClab and ACCcom are shown in Fig. 4.2. The diffractograms of both ACC materials demonstrate a turbostratic disorder (i.e. random orientation among the stacked hexagonal-structured graphene sheets). Therefore, the in-plane crystallographic structure of the graphene layers and their stacking are considerably dis-

torted [88,89]. The diffraction peak at (002) stems from the (001) crystallographic plane and the peak at $\sim 45°$ can be associated to the (100)/(101) crystallographic plane [88]. The origin of the first peak between 15° and 20° could not be determined.
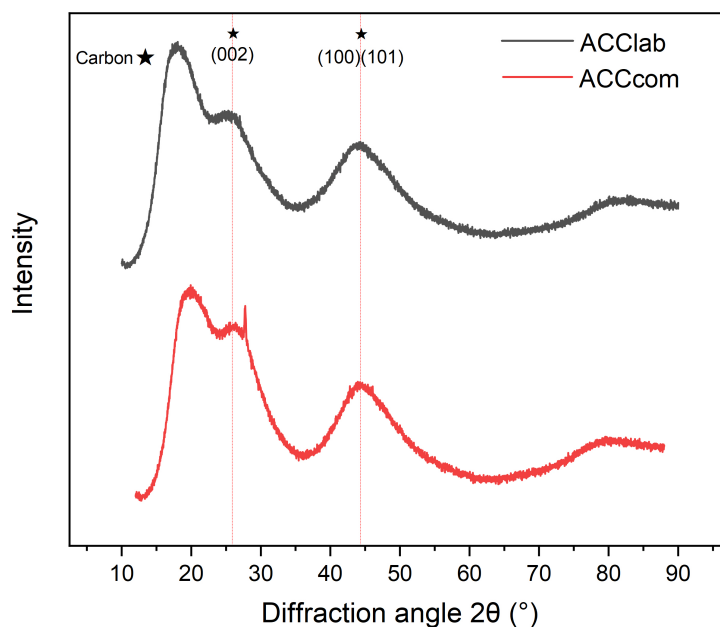

Fig. 4.2. X-ray diffractograms of vacuum-treated and grinded ACClab and ACCcom samples.

The materials also differ regarding their structural integrity. On the one hand, ACClab stays a refractory cloth even when cut into small pieces of less than 1 cm². On the other hand, ACCcom falls apart into fibers when cut. SEM was used to investigate the structural organization of the fibers and their surface morphology. Knitting was used as fabrication method for both cloth precursors as indicated in Fig. 4.3a and Fig. 4.3b. In Fig. 4.3c, the fibers of ACClab are shown at a magnification of 1000x, indicating that the surface of its fibers is smooth and even. The same can be found for the fibers of ACCcom at higher magnifications as presented in Fig. 4.3d.
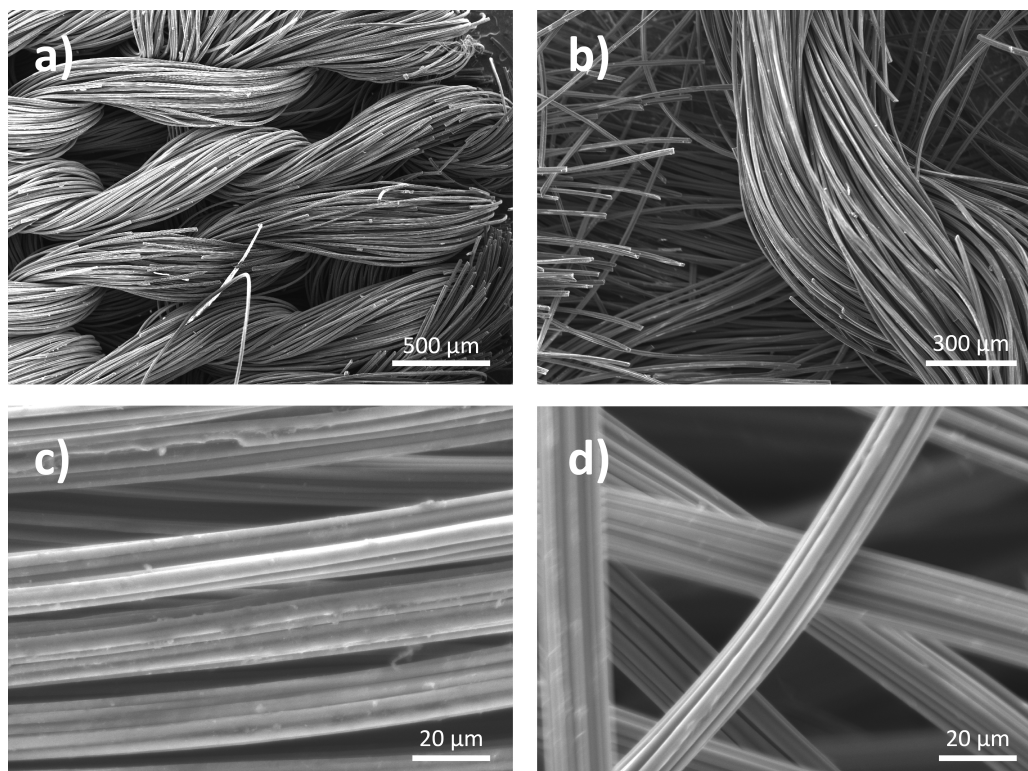
Fig. 4.3. SEM images of ACClab (a and c) and ACCcom (b and d) in different magnifications.

4.2 Synthesis of preceramic polymers

By mixing HTT1800 with Ni- and Co-based organometallics it was possible to obtain 5 different samples with different ratios of Si/Ni and Si/Co, respectively. Their physical appearance (i.e. state and colour) are summarized in Table 4.1. Both Co samples (i.e. ratios 2.5 and 5) are viscous liquids with a dark bluish colour as visible in Fig. 4.4a and Fig. 4.4b. Some Ni samples, on the other hand, appear as clay (ratio 5 - Fig. 4.4d and ratio 10 - Fig. 4.4e). The Ni sample with ratio 2.5 consists of loose flakes as observable in Fig. 4.4c. Moreover, the colour changes are more pronounced for the Ni samples as indicated by Fig 4.4c-e.

Table 4.1: Appearance and CY of the fabricated preceramic precursors of different Si/metal ratios.

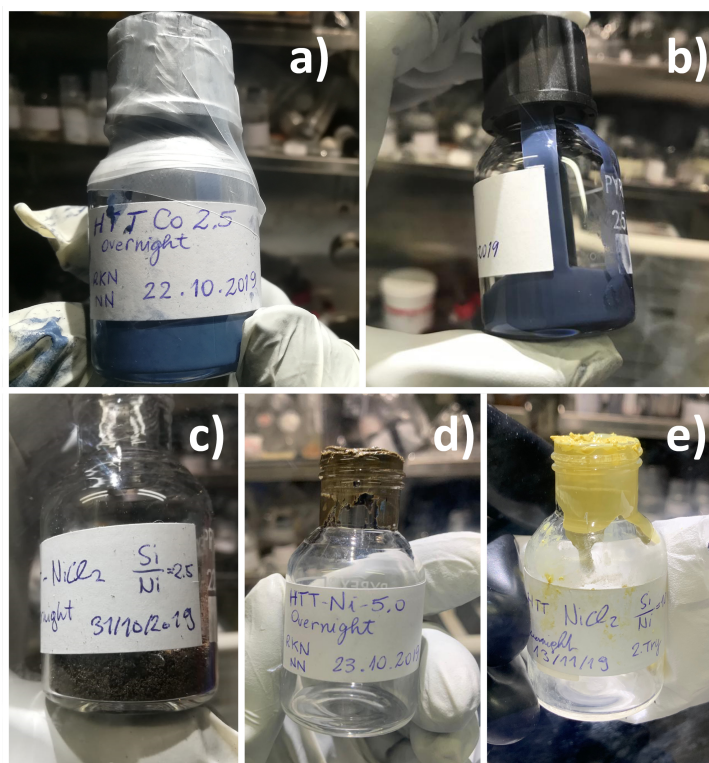| Precursor	Si/M Ratio	Appearance	Colour	CY
HTT-Co	2.5	Viscous liquid	Blue	66%
HTT-Co	5	Viscous liquid	Blue	70%
HTT-Ni	2.5	Flakes	Black	50%
HTT-Ni	5	Clay	Brown	66%
HTT-Ni	10	Clay	Yellow	76%

Fig. 4.4. Physical appearance of different HTT-Co and HTT-Ni ratios: a) HTT-Co-2.5, b) HTT-Co-5, c) HTT-Ni-2.5, d) HTT-Ni-5 and e) HTT-Ni-10.

By treating a preceramic polymer at high temperatures it will transform into a ceramic [90]. Polysilazane preceramic polymers in particular are used to create silicon carbonitride (SiCN) ceramics [91]. To study the composition changes at elevated temperatures and especially to find out at which temperature the polymer-to-ceramic conversion is finished, TGA measurements combined with mass spectrometry yield a reliable indication. Furthermore, mass spectrometry shows which volatile species evolve at elevated temperatures. In Fig. 4.5a the results of the TGA analyses are summarized. The preceramic polymer samples are compared to the TGA curve of pure HTT1800 (blue curve). It can be seen that the higher the silicon-to-metal ratio (i.e. less amount of organometallic) the higher the CY. Consequently, the smaller is the loss in mass during pyrolysis. Since little cross-linking usually results in a low CY [92], the results presented in Fig. 4.5a indicate that the addition of organometallic to the polymer weakens the cross-linking effect, which leads to a higher loss in mass. A similar behaviour regarding the formation of volatile organometallic species during TGA was found by Corriu et al. for other polymers [93]. Furthermore, the low CY of HTT-Ni-2.5 stands out. This behaviour might be attributed to a non-finished reaction of HTT1800 with $NiCl_2$. Consequently, some chlorine from the $NiCl_2$ was still trapped in the sample. Due to the release of chlorine during TGA, the CY is reduced.

The results of the mass spectrometry analysis of pure HTT1800 are plotted in Fig. 4.5b. It can be seen that two major peaks at ~ 350 °C and ~ 550 °C are observable. Its

pyrolysis is accompanied by the evolution of gaseous H_2 (mass-to-charge ratio (m/z) = 2), CH_4 (m/z = 16), NH_3 (m/z = 17) as well as several oligomer fragments with higher mass-to-charge ratio (m = 26 - 30). The peaks in the mass spectrometry curve of HTT-Ni-5 are partially shifted as observable in Fig. 4.5c. The first major peak appears at ~ 250 °C (rather than 350 °C for HTT1800) and the second peak remains at ~ 550 °C. Fig. 4.5d shows the mass spectrometry data of HTT-Co-5. The same peak shift (250 °C rather than 350 °C for HTT1800) can also be found for this sample and the second peak at ~ 550 °C appears in a narrower range than for HTT1800 and HTT-Ni-5. The Co and Ni reference sample seem to lose the same gaseous species as HTT1800 and also do not show any formation of unexpected compounds.

The peak shift to 250 °C indicates that the mixing of HTT1800 with organometallics shifts the beginning of the cross-linking process to lower temperatures. Furthermore, the TGA curves and the mass spectrometry data indicate that no real change in composition occurs above 700 °C. Consequently, it can be assumed that the polymer-to-ceramic conversion should be complete by applying a pyrolysis temperature of 700 °C.
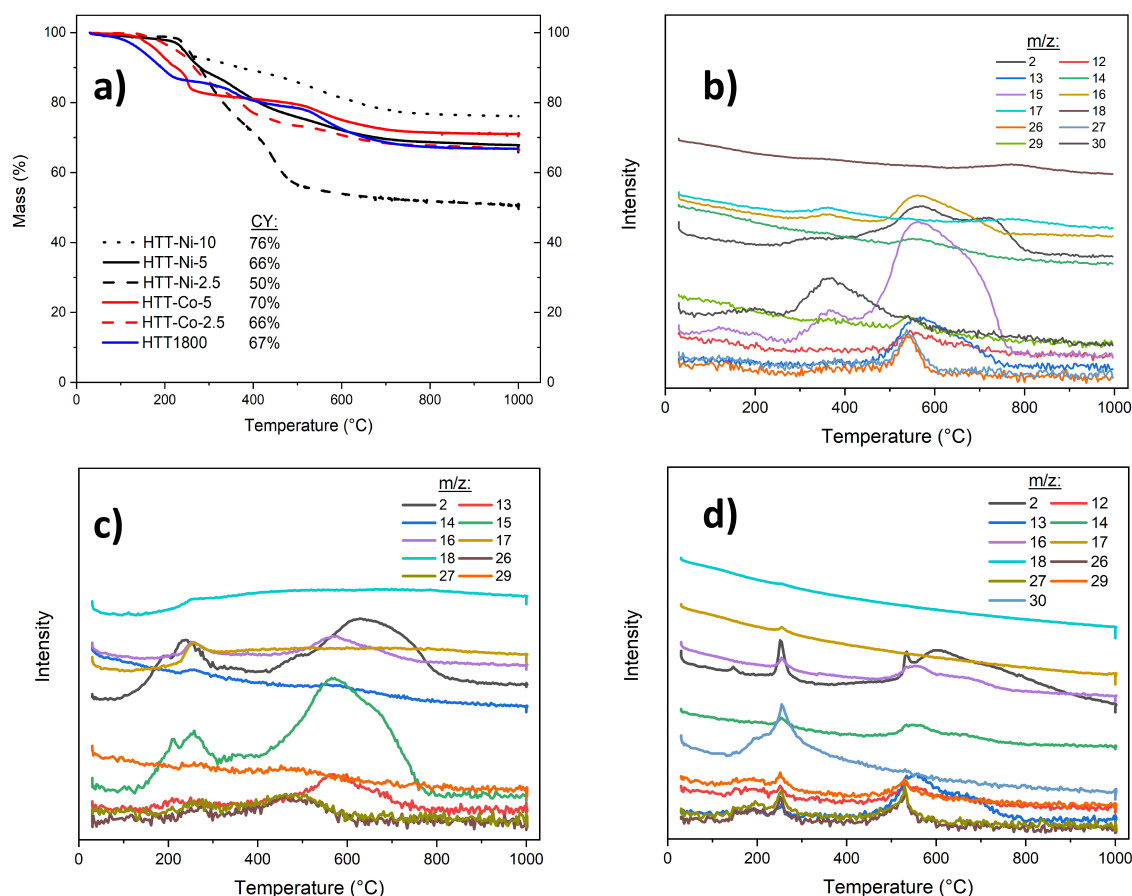

Fig. 4.5. a) TGA curves obtained in argon for the preceramic polymers in different ratios compared to pure HTT1800. The CY is shown in the legend. b) Mass spectrometry data of pure HTT1800. c) Mass spectrometry data of HTT-Ni-5. d) Mass spectrometry data of HTT-Co-5. M/z stands for the mass-to-charge ratio.

Fig. 4.6 shows the results of the FTIR measurements for both preceramic polymer samples with a ratio of 5 compared to HTT1800. It can be seen that the major bonds of the polymer chain Si-N (950 cm^{-1}), Si-H (2160 cm^{-1}) and Ni-H (3390 cm^{-1}) appear in all samples with similar intensities [84]. The methyl group (1410 and 2980 cm^{-1}) and vinyl group (1600 and 2900 cm^{-1}) can also be found in all samples [84]. The HTT-Ni-5 sample was crushed into a powder and embedded in a KBr matrix due to its non-liquid state. HTT-Co-5 and pure HTT1800 were both placed as droplets between two KBr pellets because of their liquid state. Since very similar sample masses were used, the peak height can be seen as quantitative adumbration. Because all peaks of HTT-Ni-5 (Fig. 4.6a) and HTT-Co-5 (Fig. 4.6b) show a very similar transmittance as their counterparts of pure HTT1800, it can be assumed that the bonding before and after reacting with NiCl$_2$ and CoCl$_2$ is hardly altered. Since no peaks are vanishing after reacting with either NiCl$_2$ or CoCl$_2$, it can be presumed that neither Ni nor Co get integrated into the polymeric matrix. Furthermore, only some minor peaks appear after the reaction in both samples at ~ 1400 cm^{-1} and at ~ 3300 cm^{-1}. Since chlorine is the only substance that appears in both, NiCl$_2$ and CoCl$_2$, it can be assumed that these two peaks are forming due to an interaction of chlorine with the matrix.
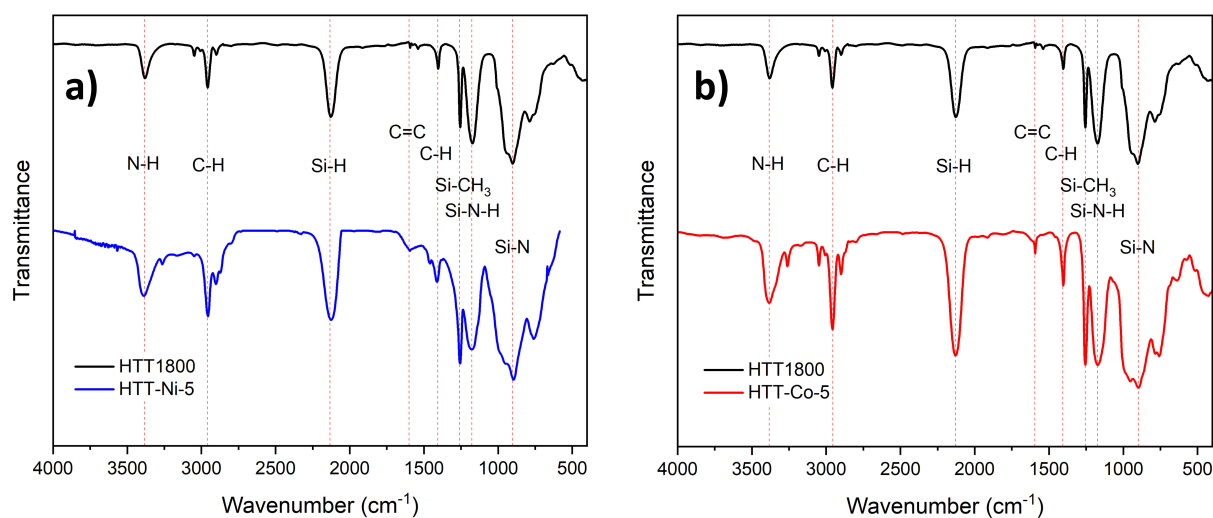
Fig. 4.6. a) FTIR spectra of HTT-Ni-5 compared to HTT1800 in a KBr matrix. b) FTIR spectra of HTT-Co-5 compared to HTT1800 in a KBr matrix.

4.3 Polymer-to-ceramic conversion

The choice of the pyrolysis temperature is a crucial parameter to maximise the performance of the nanocomposites. This is because the temperature is directly affecting the polymer-to-ceramic conversion and the retention of the nanopore network of the ACC ma-

terials. As indicated by the results of TGA and mass spectrometry, a pyrolysis temperature of 700 °C seems sufficient to complete the polymer-to-ceramic conversion. Therefore, all pyrolyses were carried out at this temperature.

The X-ray diffractograms of the ceramic samples are summarized in Fig. 4.7a for the Ni samples and in Fig. 4.7b for the Co samples. The graphs show that the Ni samples in general lead to less noise compared to the Co samples. Furthermore, it can be concluded that the higher the silicon-to-metal ratio (i.e. less organometallic), the less pronounced are the peaks of pure Ni and Co. This means that the more Co or Ni was used for the reaction, the higher is its amount in crystalline form in the final ceramic. Other stoichiometric and non-stoichiometric phases are also observable in both figures, however the presence of NH_4Cl is surprising and was not intended.
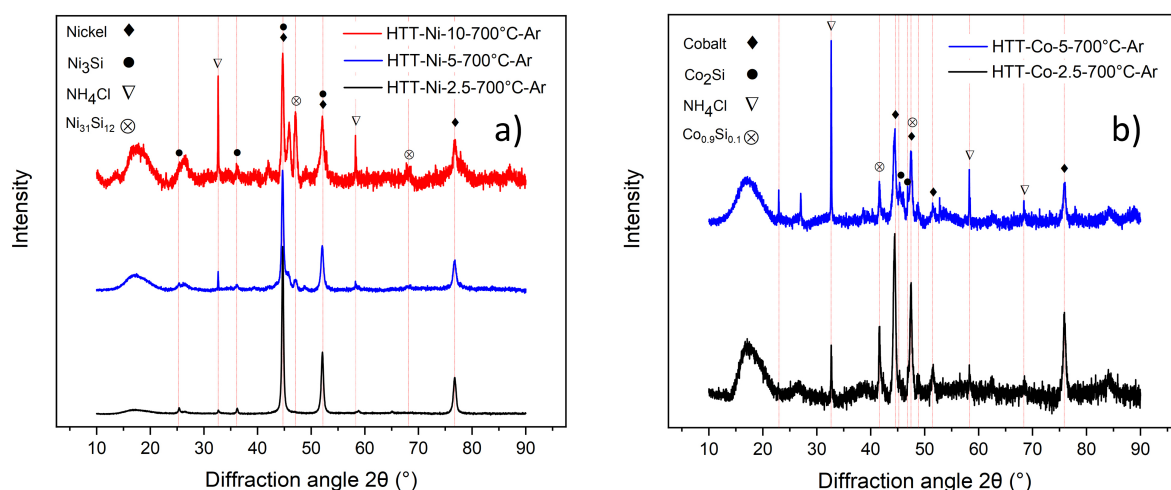

Fig. 4.7. a) X-ray diffractograms of HTT-Ni of ratio 2.5, 5 and 10. b) X-ray diffractograms of HTT-Co of ratio 2.5 and 5.

Fig. 4.8a shows a SEM image of HTT-Ni-5 at low magnification. The surface looks relatively even but shows some particles (appearing bright in the image) on its surface. Although the nature of those bright particles was not determined by EDX, it is reasonable that those particles consist of nickel or a nickel-silicon phase. By considering the FTIR results, it is unlikely that the Ni got embedded in the matrix. Therefore, most of the nickel appears to be capsuled as particles below the surface. Fig. 4.8b shows the EDX pattern of HTT-Ni-5 as well as the average composition of the sample, which is depicted in the pie chart. By dividing the value of Si by the value of Ni, the average ratio of the sample was calculated to ~ 3.7. This means that, close to the surface, the amount of Ni is lower than the desired value. This is either a consequence of the synthesis process or an instrumental error because of the low penetration depth of EDX [94].

The EDX results of HTT-Co-5 show similar characteristics, as depicted in Fig. 4.9b. However, its SEM image (Fig. 4.9a) appears smoother than the one of its Ni counterpart

and there is no indication of other species on the surface. Fig. 4.9b shows the results of the EDX measurements for HTT-Co-5. By dividing the Si value by the Co value from the average composition values depicted in the pie chart, a Si/Co ratio of ~ 4.1 can be calculated. Therefore, the amount of Co also seems to be lower than intended. This could again be attributed to the limited penetration depth of EDX [94]. Since there is no indication of Co on the surface, it can be assumed that Co is capsuled below the surface or integrated within the ceramic matrix.
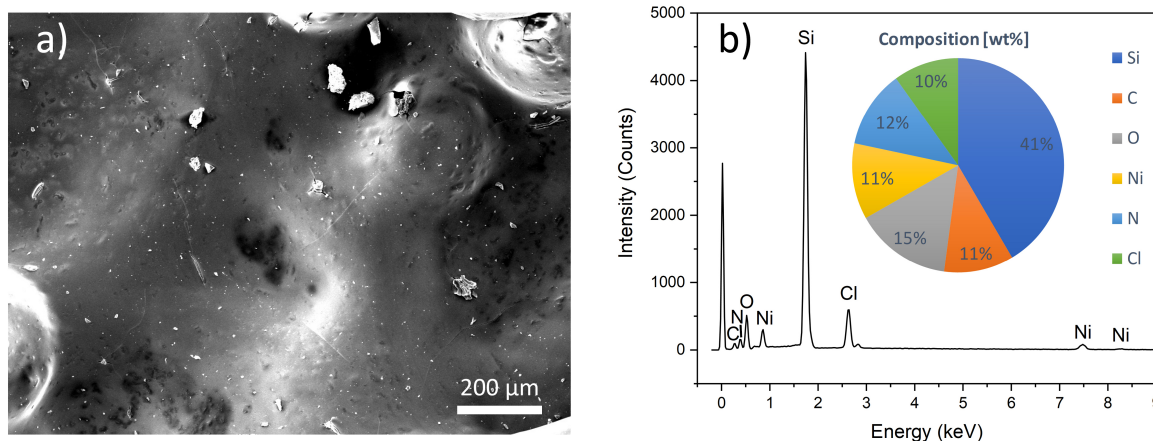

Fig. 4.8. a) SEM image of HTT-Ni-5 at low magnification. b) EDX spectrum of HTT-Ni-5 including the relative amounts (%wt) of elements in the sample.
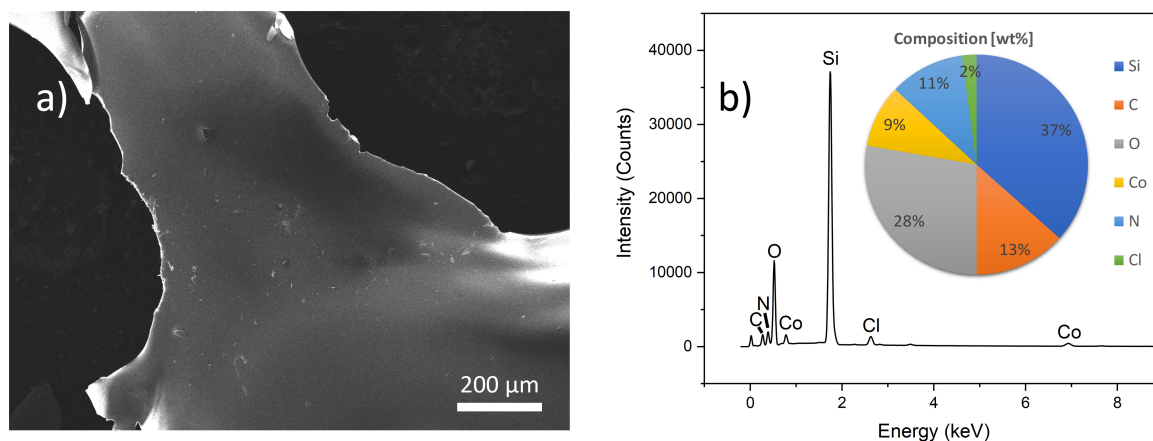

Fig. 4.9. a) SEM image of HTT-Co-5 at low magnification. b) EDX spectrum of HTT-Co-5 including the relative amounts (%wt) of elements in the sample.

4.4   Impregnation

4.4.1   Synthesis of impregnation polymers

By impregnating 2 different ACC materials (i.e. ACClab and ACCcom) with 5 different preceramic precursors, 10 different samples for subsequent pyrolysis (i.e. formation of nanocomposites) were produced. The main parameters of each impregnation (i.e. mass ratio of PDC/ACC, concentration of preceramic precursor in toluene) are summarized in Table 4.2. The table also shows the subsequently used denomination of the impregnated samples. It has to be noted that due to a process error the mass ratio of preceramic polymer/ACC was 2 for the HTT-Ni-5 samples (ACClab and ACCcom) rather than 1.4 for all other samples. As a result, the HTT-Ni-5 samples came in contact with more impregnation material.

Table 4.2: Summary of the impregnated samples including their subsequently used denominations. The polymer-to-ACC mass ratio as well as the concentration (denoted as Concen.) of polymer in toluene are shown.

Ceramic	Ratio	ACC	Denomination	Polymer/ACC	Concen.
HTT-Ni	2.5	ACClab	HTT-Ni-2.5-ACClab	1.4	0.5 g mol^{-1}
HTT-Ni	2.5	ACCcom	HTT-Ni-2.5-ACCcom	1.4	0.5 g mol^{-1}
HTT-Ni	5	ACClab	HTT-Ni-5-ACClab	2.0	0.3 g mol^{-1}
HTT-Ni	5	ACCcom	HTT-Ni-5-ACCcom	2.0	0.3 g mol^{-1}
HTT-Ni	10	ACClab	HTT-Ni-10-ACClab	1.4	0.15 g mol^{-1}
HTT-Ni	10	ACCcom	HTT-Ni-10-ACCcom	1.4	0.15 g mol^{-1}
HTT-Co	2.5	ACClab	HTT-Co-2.5-ACClab	1.4	0.3 g mol^{-1}
HTT-Co	2.5	ACCcom	HTT-Co-2.5-ACCcom	1.4	0.3 g mol^{-1}
HTT-Co	5	ACClab	HTT-Co-5-ACClab	1.4	0.3 g mol^{-1}
HTT-Co	5	ACCcom	HTT-Co-5-ACCcom	1.4	0.3 g mol^{-1}

4.4.2   Impregnation with preceramic polymers

Fig. 4.10 summarizes the physical appearance of the materials after the impregnation process exemplary for all 4 samples with a ratio of 5. Fig. 4.10a and Fig. 4.10c show HTT-Ni-5-ACClab and HTT-Ni-5-ACCcom, respectively. As already discussed, ACCcom is characterized by a worse structural integrity, which is evident by comparing the figures. The brownish stains are attributed to the impregnation procedure, where some polymer segregates to the bottom of the flask. Consequently, the ACC pieces that are on the bottom are in contact with a higher amount of polymer. By comparing the HTT-Ni figures to HTT-Co-5-ACClab (Fig. 4.10b) and HTT-Co-5-ACCcom (Fig. 4.10d), it can be observed that the Co samples do not show these brownish stains. The reason for this

can be found in the ratio of polymer to ACC material that was used for impregnation. As mentioned previously, the ratio for the HTT-Ni-5 samples is higher (i.e. 2) than for the other samples (i.e. 1.4). Furthermore, the ACCcom shows an even worse structural integrity with the Co sample (Fig. 4.10d). This is because the cloth has not been cut in such small pieces for HTT-Ni-5 than for all the other samples. Consequently, the smaller the pieces, the more the ACCcom decomposes into fibres.
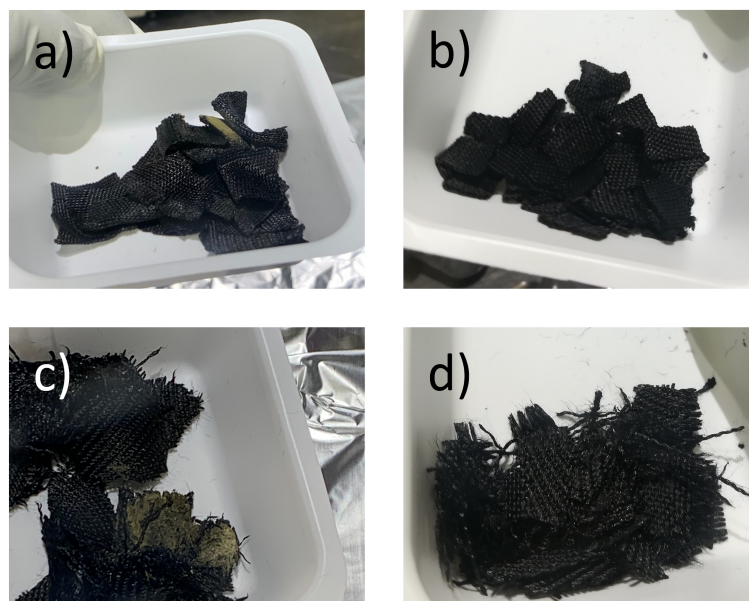

Fig. 4.10. Appearance of the used ACC materials with different organometallics (i.e. $NiCl_2$ and $CoCl_2$) after impregnation shown exemplary for ratio 5: a) HTT-Ni-5-ACClab, b) HTT-Co-5-ACClab, c) HTT-Ni-5-ACCcom and d) HTT-Co-5-ACCcom.

4.5   Characterization of the nanocomposites

The fibers sustained the heat-treatment of up to 700 °C in argon without any obvious change of their physical appearance. The appearance of the newly-formed nanocomposites is shown exemplary for HTT-Co-2.5-ACClab in Fig. 4.11. However, when small loads were applied by hand, the pieces fractured rapidly. Therefore, the heat treatment led a strongly increased brittleness of the samples, which is most likely due to the non-flexible nature of the SiCN ceramics that formed onto the fibres [95]. Thus, the flexibility of the nanocomposites is significantly reduced.
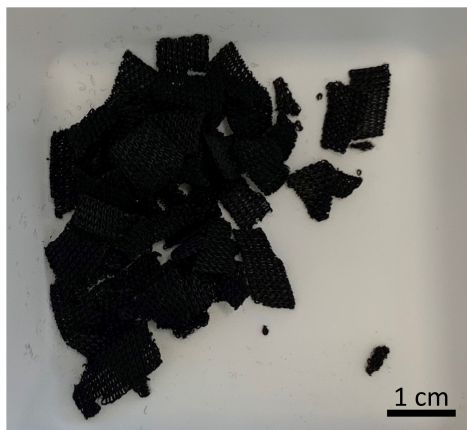
Fig. 4.11. Appearance of nanocomposites after pyrolysis shown exemplary for HTT-Co-2.5-ACClab.

The results of the Raman measurements are summarized in Fig. 4.12. For some of the samples no indication of any pronounced peak is observable as depicted in Fig. 4.12b. A clear trend which samples (and which ratios) show this behaviour could not be determined. The origin of this effect might be attributed to fluorescence caused by the impregnation material, even though further studies would be necessary for clarification. All samples with pronounced Raman activity (Fig. 4.12a) show peaks at a Raman shift of roughly 1350 cm^{-1} and at roughly 1600 cm^{-1}. Typically, SiCN ceramics derived from polysilazanes also contain some excess carbon [96]. Thus, the first peak visible in Fig. 4.12a can be associated with the defect-activated D-band of carbon at $\sim$ 1338 cm^{-1}, which appears as a result of the disordered structure. The second peak can be associated with the bond stretching vibration of sp^2 hybridized carbon atoms in a two-dimensional hexagonal lattice (i.e. graphitic G band at $\sim$ 1593 cm^{-1}) [97, 98]. Two small peaks at higher frequencies (i.e. 2500 - 3000 cm^{-1}) are only observable for HTT-Co-2.5-ACClab and pure ACClab. The first peak at $\sim$ 2686 cm^{-1} can be associated with the 2D band as a result of the double resonance transition due to the generation of two opposite phonon momentum [99, 100]. The second peak can be related to the D + D' band ($\sim$ 2890 cm^{-1}), which results from defect activation with different phonons (i.e. transversal optical phonons for D and longitudinal optical phonons for D') [99, 101].
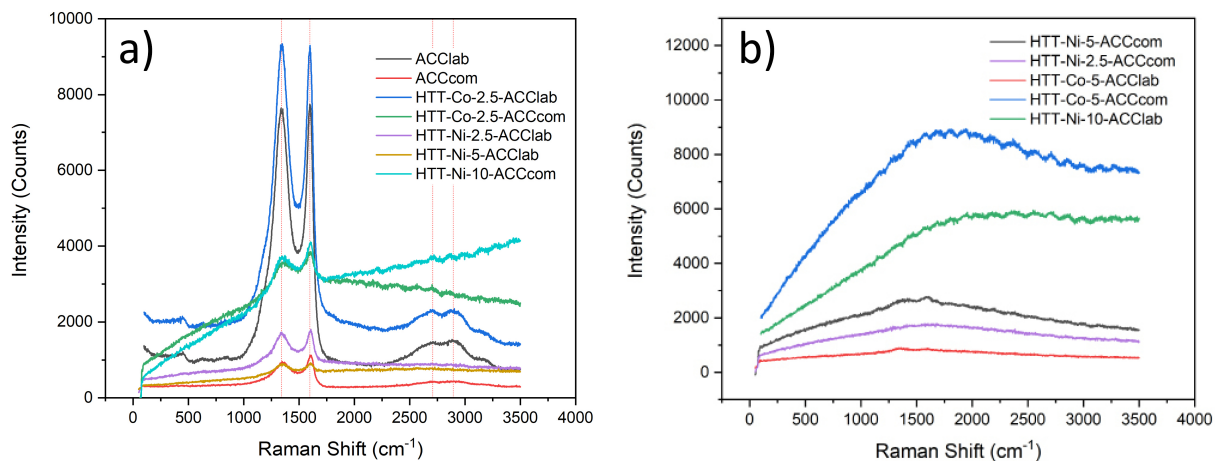
Fig. 4.12. Raman spectra of the synthesized nanocomposites and the pure ACCs. a) Samples which feature pronounced peaks. b) Samples that do not show any pronounced peak and a lot of noise.

X-ray diffractograms of the ACClab-based nanocomposites are shown in Fig. 4.13 for the Ni-ACClab samples (a) and the Co-ACClab samples (b), respectively. All nanocomposites were vacuum-treated before XRD was performed to examine the influence of such a treatment on the materials. Both figures illustrate that the vacuum treatment led to the disappearance of NH_4Cl in all nanocomposites. Furthermore, in Fig. 4.13a it can be observed that all Ni-Si compounds have vanished and only the pure Ni peaks remain. In Fig. 4.13b some Co-Si compounds remain present additionally to the pure Co peaks. The carbon peak at approximately 26° is present in all samples, which corresponds to the (002) reflection [13]. Furthermore, the (100)/(101) reflection that was present in the pure ACC samples at 45° could also be present in the nanocomposites. However, the dominant Co- and Ni-peaks overlay; it is therefore impossible to distinguish them from an eventual carbon peak.
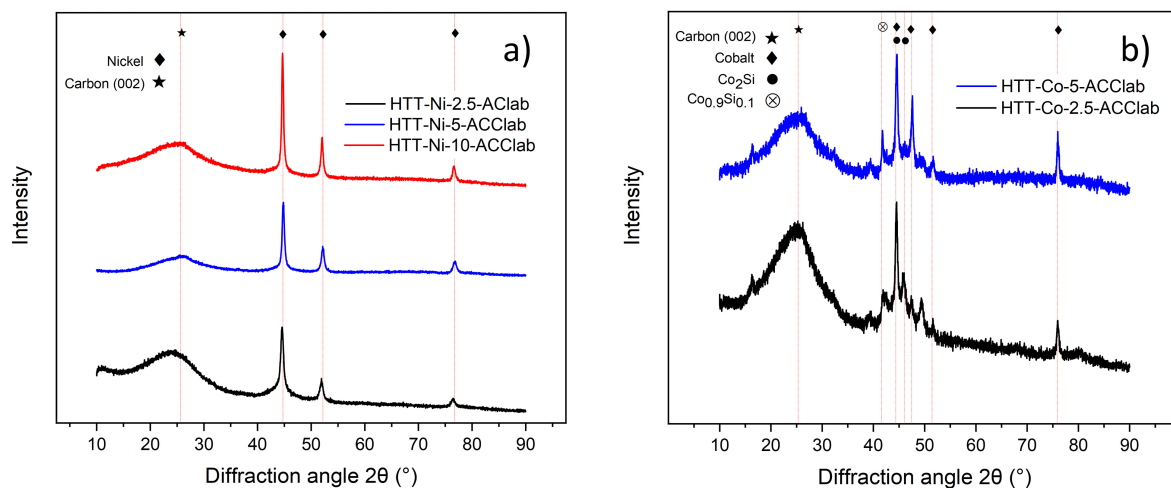
Fig. 4.13. X-ray diffractograms of a) Ni-ACClab-based nanocomposites of ratio 2.5, 5 and 10 and b) Co-ACClab-based nanocomposites of ratio 2.5 and 5.

SEM images of HTT-Ni-5-ACClab (Fig. 4.14a-c) and HTT-Co-5-ACClab (Fig. 4.14d-f) at different magnifications are displayed in Fig. 4.14. Even at low magnifications it is observable that the surface of both samples is partially covered with the PDCs (compare Fig. 4.3a). However, the impregnation is very inhomogeneous. Fig. 4.15 depicts SEM images of HTT-Ni-5-ACCcom (Fig. 4.15a-c) and HTT-Co-5-ACCcom (Fig. 4.15d-f) at different magnifications. The images show similar results as for its ACClab counterparts. Due to the higher amount of HTT-Ni-5 that was used as impregnation material, a higher amount of the ACClab and ACCcom surface is covered, which can be observed in Fig. 4.14a-c and Fig. 4.15a-c, respectively. It can be concluded that due to the inhomogeneous impregnation, the chosen synthesis procedure is not ideal to fabricate homogeneously coated nanocomposites. Additionally, lots of cracks are observable in the different SEM images that indicate the brittle nature of the nanocomposites.
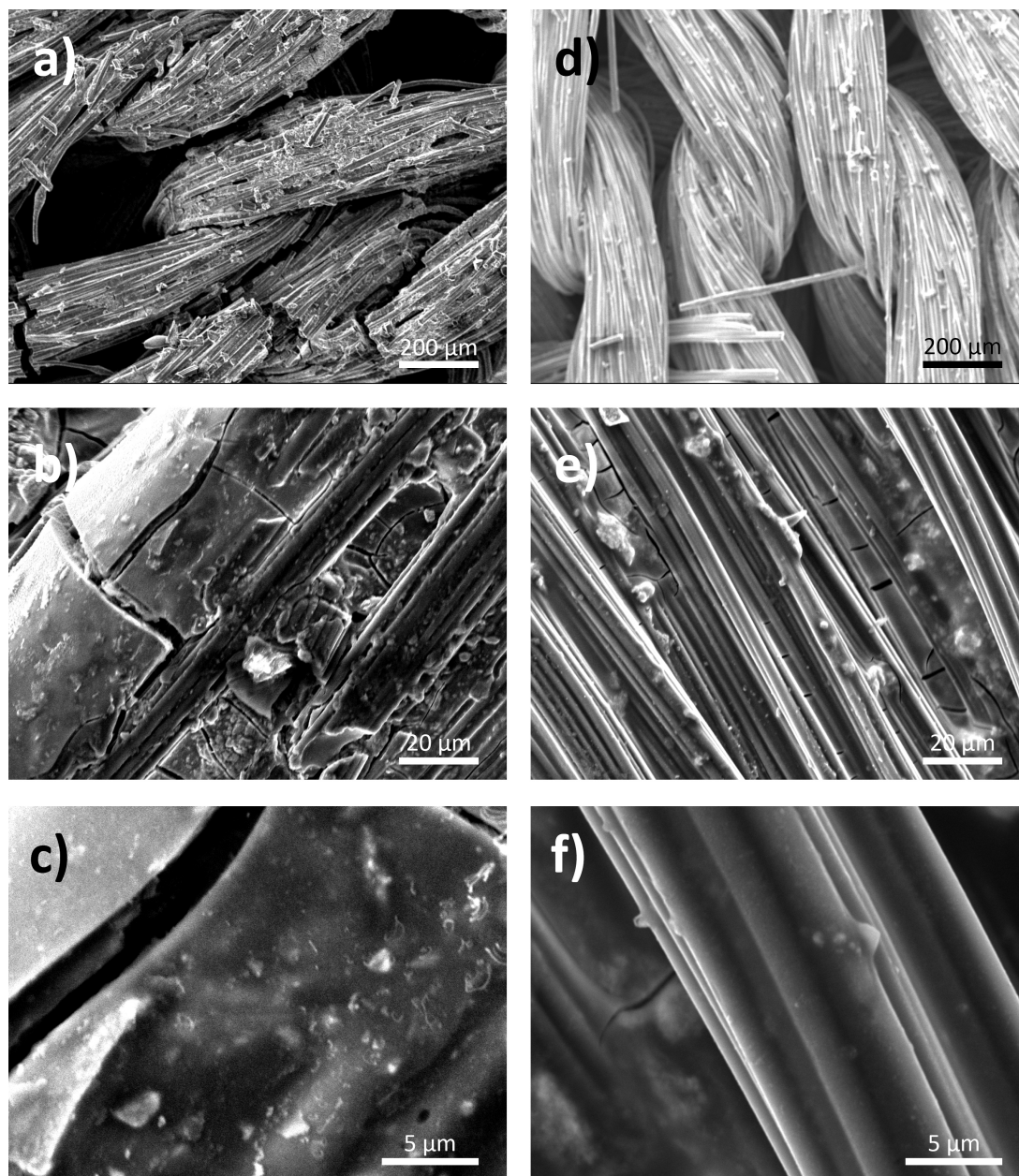
Fig. 4.14. SEM images of ACClab-based nanocomposites. a-c) HTT-Ni-5-ACClab at different magnifications. d-f) HTT-Co-5-ACClab at different magnifications.
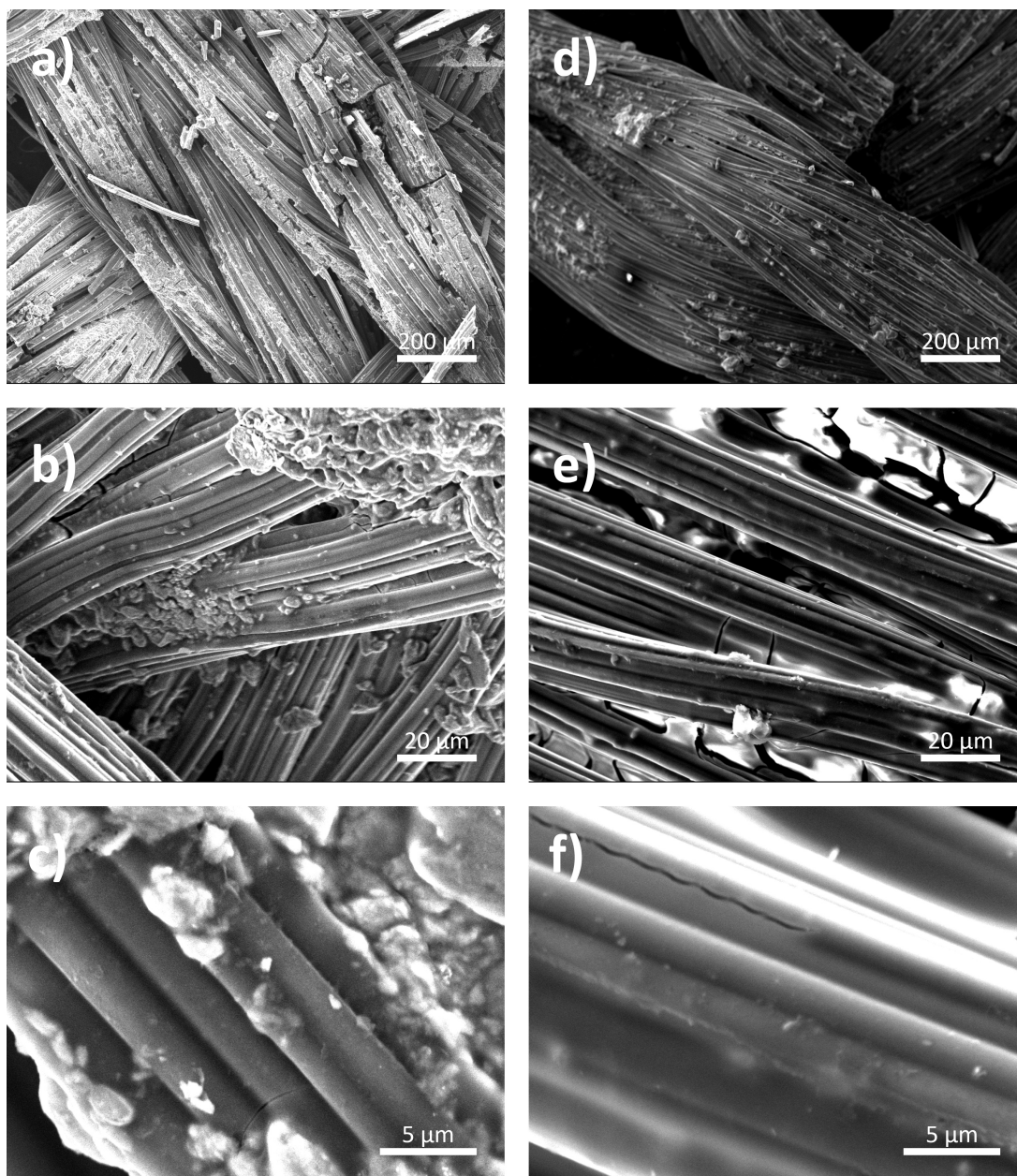
Fig. 4.15. SEM images of ACCcom-based nanocomposites. a-c) HTT-Ni-5-ACCcom at different magnifications. d-f) HTT-Co-5-ACCcom at different magnifications.

The N_2 ad-/desorption isotherms at 77 K are displayed in Fig. 4.16. The results indicate that the absorbed N_2 volume of all nanocomposites is below the value of pure ACClab. This is in accordance to the reduced S_{BET} and S_{DFT} that are presented in Table 4.3. Fig. 4.16 illustrates that all isotherms exhibit typical type I behaviour as proposed by IUPAC [51]. ACClab exhibits type Ia behaviour (i.e mainly micropores), while all nanocomposites display type Ib behaviour (i.e. broader PSD), which leads to a less steep increase and therefore to a shorter plateau in the isotherm [51, 57]. Since no hysteresis loop between adsorption and desorption curve is observable for any sample, no indication of mesoporosity is found [13]. All nanocomposites show a slight increase at relative pressures close to unity ($p/p_0 = 0.99$), which could be attributed to condensation

in macropores and adsorption onto external surfaces [13], even though the effect seems to be very weak. The TPV, summarized in Table 4.3, was calculated using the single-point Gurvich rule and the QSDFT method. The obtained values decreased by $\sim 50\%$ and more for all nanocomposites compared to the pure ACClab. Both methods (i.e. Gurvich and the QSDFT) led to similar results as observed in Table 4.3.
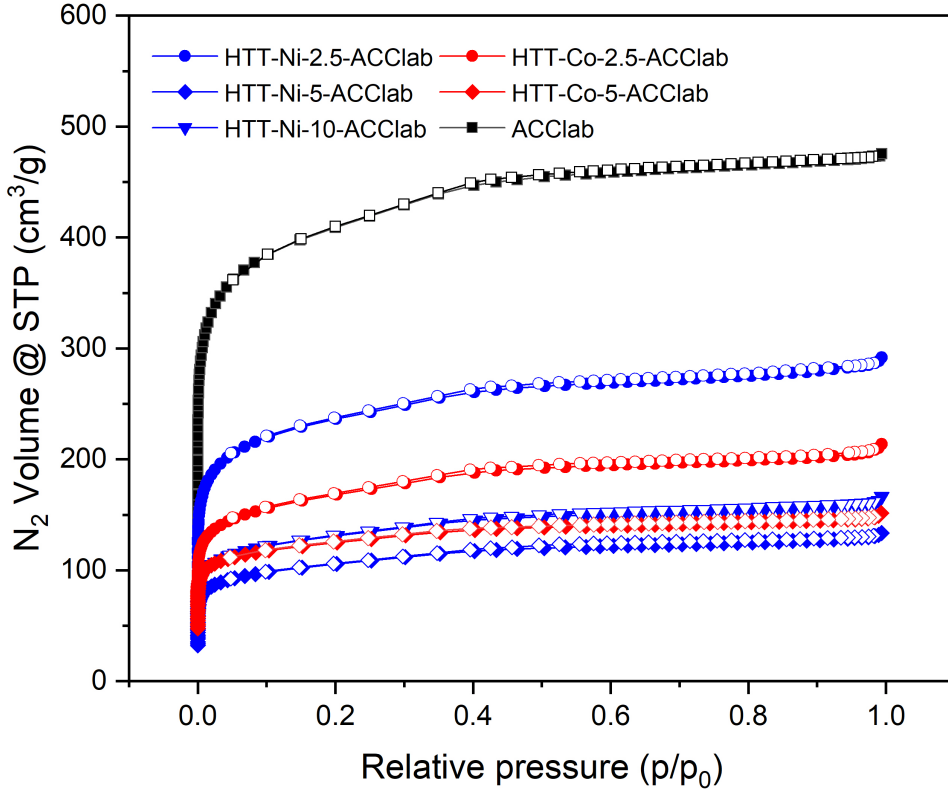
Fig. 4.16. N_2 ad-/desorption isotherms recorded at 77 K for all ACClab-based nanocomposites compared to pure ACClab, starting from a relative pressure of 10^{-6}.

Fig. 4.17 demonstrates the PSD. In Fig. 4.17a, the cumulative pore volume for all ACClab-based samples compared to pure ACClab, calculated using a slit-pore model based on the QSDFT method, is illustrated. The graph shows the same trend as the calculated values of the TPV in Table 4.3. It can be seen that materials with ratio 5 show the lowest total pore volume at all pore widths. HTT-Ni-5-ACClab was impregnated with a higher amount of impregnation material. Since it has the lowest cumulative pore volume, it can be concluded that the higher amount of impregnation material led to the low TPV as a result of pore blocking [102]. In Fig. 4.17b, the differential pore volume for all ACClab-based samples compared to pure ACClab is illustrated. The graph features a sharp peak that is only observable for pure ACClab and HTT-Ni-2.5-ACClab at roughly 0.7 nm. Therefore, the process led to the vanishing of this peak in all other samples,

which also led to a lower TPV as indicated by Fig. 4.17 and Table 4.3. All materials show a steep increase at even lower pore widths. Although this indicates that all samples contain pores with sizes in the ultramicropore (pore size < 0.7 nm) and supermicropore (0.7 < pore size < 2 nm) range [56], the data suggests that N_2 cannot access pores with widths below 0.6 nm. Consequently, CO_2 ad-/desorption measurements would need to be conducted to fully resolute the PSD. The reason is that CO_2 isotherms are obtained at higher pressures and temperatures, which leads to a higher diffusion. Consequently, pores as small as 0.4 nm can be accessed [51]. Table 4.3 also summarizes the APW, estimated for an infinitely extended slit-like pore. All materials feature a similar APW of roughly 0.7 - 0.9 nm, which corresponds to a pore size in the supermicropore range [56].

Table 4.3: Summary of the ad-/desorption measurements. S_{BET} and S_{DFT} are presented as well as the TPV using the Gurvich rule (calculated for pores smaller than 55 nm at a relative pressure of 0.96) and the DFT method (calculated using the pure carbon kernel based on the slit-pore model). APW was estimated for an infinitely extended slit-like pore.

Sample	S_{BET}	S_{DFT}	$TPV_{Gurvich}$	TPV_{DFT}	APW_{DFT}
	m^2/g	m^2/g	cm^3/g	cm^3/g	nm
ACClab	1539	1641	0.73	0.68	0.83
HTT-Ni-2.5-ACClab	884	911	0.44	0.41	0.90
HTT-Co-2.5-ACClab	622	697	0.32	0.30	0.86
HTT-Ni-5-ACClab	392	471	0.20	0.19	0.85
HTT-Co-5-ACClab	469	542	0.23	0.21	0.74
HTT-Ni-10-ACClab	488	539	0.25	0.23	0.86

These results indicate that the impregnation of ACC with PDCs blocked the pores partially with ceramic or metal particles or that the pyrolysis destroyed parts of the microporosity. However, the similar shape of all isotherms strengthens the assumption that the pore network stayed intact during the whole procedure. Thus, potential pore blocking is most likely the reason for the decreased SSA and TPV of all nanocomposites [17, 102, 103].

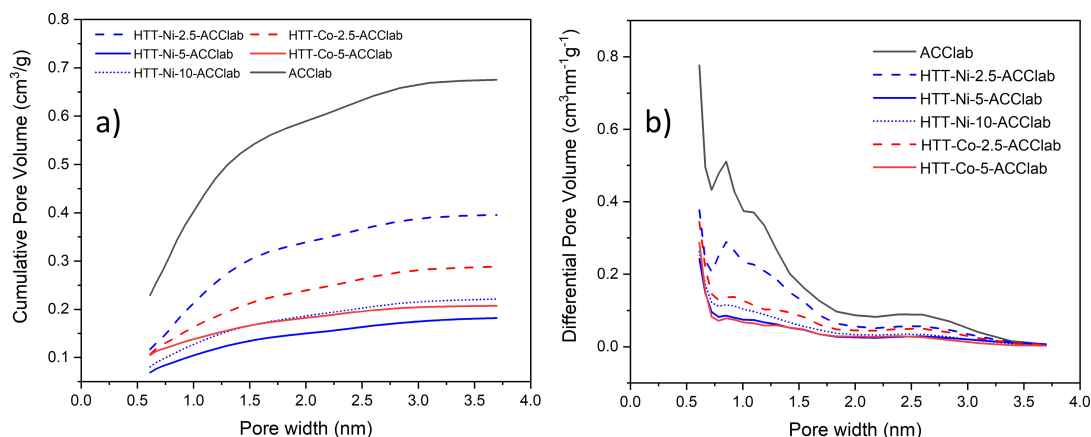**Fig. 4.17.** a) Cumulative pore volume of all ACClab-based nanocomposites compared to pure ACClab, starting from a relative pressure of 10^{-6} using N_2 at 77 K. b) Differential pore volume of all ACClab-based nanocomposites compared to pure ACClab, starting from a relative pressure of 10^{-6} using N_2 at 77 K. The N_2-carbon equilibrium transition kernel at 77.4 K for slit pores was used for the calculations.

To analyze the suitability of the fabricated nanocomposites in energy storage devices, different electrochemical measurements were performed. The results of the CV measurements are summarized in Fig. 4.18. Even though the CV measurements were performed with all ACClab-based nanocomposites, only some of them demonstrated a supercapacitor-like behaviour. Fig. 4.18d shows the CV results exemplary for HTT-Ni-5-ACClab, but a similar behaviour was also observed for HTT-Co-5-ACClab. The calculated capacitance values increase strongly at very low scan rates with hardly any hysteresis loop. This effect might be attributed to a decreased conductivity as a result of the impregnation or because of the small average pore sizes, which could hinder the ions to penetrate the pores [104]. Fig. 4.18a shows the results of the CV measurements for HTT-Ni-2.5-ACClab, HTT-Ni-10-ACClab and HTT-Co-2.5-ACClab compared to pure ACClab at a scan rate of 1 mV/s. The hysteresis loop for all nanocomposites is smaller than for the pure ACClab. Fig. 4.18b shows the same materials at a scan rate of 10 mV/s. The results evidence that the hysteresis is again smaller for the nanocomposite samples than for pure ACClab. Therefore, the data suggest that the impregnation with PDCs decreased the amount of energy that can be stored in the samples, which can be linked to the decreased SSA [25, 104]. Fig. 4.18c presents the CV hysteresis loops for HTT-Ni-2.5-ACClab at different scan rates, since this was the only material that behaved as a supercapacitor at all scan rates. The data indicate that a smaller scan rate leads to an increasing hysteresis (i.e. a higher energy storage capability), which is in good agreement with literature [11, 105]. This behaviour can be linked to microporosity, which leads to a decreasing ion diffusion and consequently smaller capacitance values [25]. The amount of metal particles (ratio 2.5, 5 or 10) does not have a clear impact on the results, since all

hysteresis decreased independently of the chosen ratio without any indication of a trend. Lee et al. found that the hysteresis loop increases up to a certain value with an increasing amount of metal dopant before the calculated capacitance decreases as a result of excess metal blocking the pores [106]. These findings and the results of the porosity measurements indicate that a smaller amount of impregnation material with a different amount of metal content could lead to improved cyclic voltammetry results if pore blocking can be significantly reduced.

It can be concluded that the synthesis route reduced the storage capabilities of the material and that the materials, therefore, are not suitable as electrodes for supercapacitor applications.
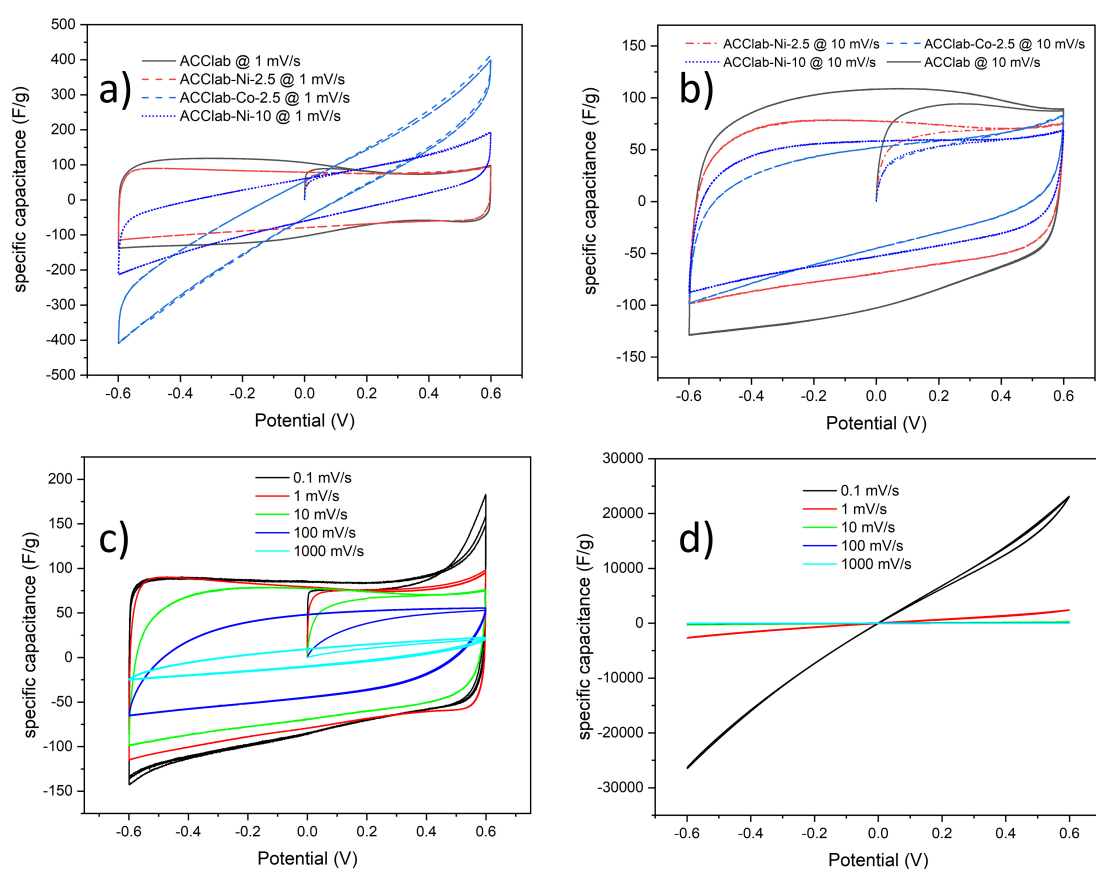
Fig. 4.18. CV curves of HTT-Ni-2.5-ACClab, HTT-Ni-10-ACClab and HTT-Co-2.5-ACClab compared to pure ACClab at a scan rate of 1 mV/s (a) and 10 mV/s (b). c) illustrates the scan rate dependence of HTT-Ni-2.5-ACClab. In d), the effect of a strong increase in capacitance with hardly any hysteresis loop with decreasing scan rate is shown exemplary for HTT-Ni-5-ACClab.

Fig. 4.19 summarizes the impedance spectroscopy results as Nyquist plots. It has to be noted, that the pure ACClab was not included in the data since its electrode size and thickness differed from the nanocomposite-based electrodes, which limits the reliability of the data strongly [107]. As a consequence of the complexity of the nanocomposite

system, the small size and non-uniform shape of the used WEs, the data should be only seen qualitatively. Fig 4.19a and Fig. 4.19b indicate that the fabricated nanocomposites show a similar EIS behaviour. The absence of a vertical line at low frequencies (which corresponds to a small Z', as shown in magnification in Fig. 4.19b) can be attributed to diffusion effects that result in a tilted line as a consequence of the microporosity of all nanocomposites [25]. All materials exhibit semicircle-shaped Nyquist curves at higher frequencies (which corresponds to higher values of Z') as illustrated in Fig. 4.19a. The radius of the curves is influenced by the amount and choice of impregnation material [108]. Fig. 4.19b, which presents the magnification of the first part of the Nyquist plot, indicates that the ESR for all nanocomposites, except for HTT-Co-5-ACClab, is similar and should therefore be hardly affected by the metal (and ratio) used in the coating. Vaquero et al. noticed that the ESR is mainly affected by the electrolyte and less by the chosen electrode material [25]. The different ESR and radius of HTT-Co-5-ACClab might be attributed to statistical deviations of the amount of impregnation material on the surface of the sample [108]. Furthermore, the measurement in general is prone to alterations of the shape, size and thickness of the used electrodes [107].
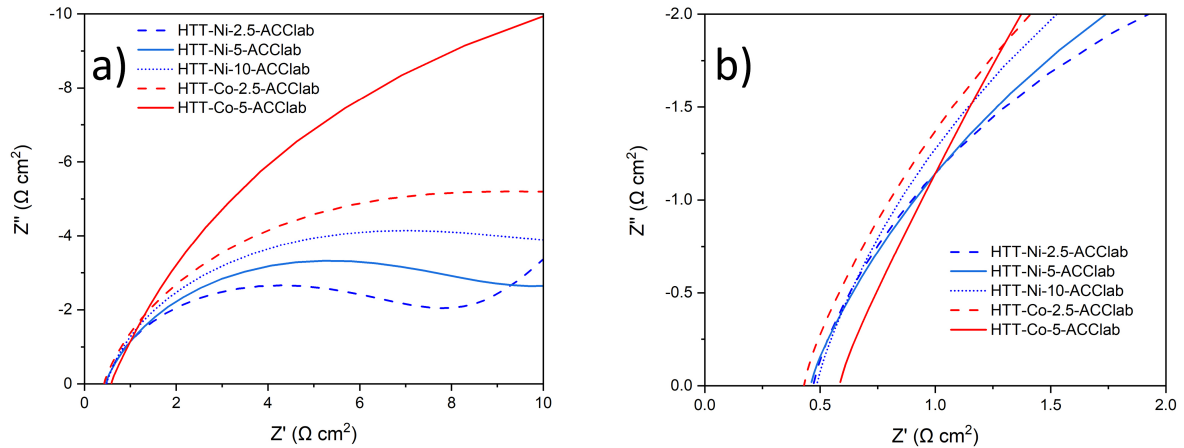

Fig. 4.19. a) Nyquist impedance plots of the fabricated nanocomposites. b) shows the magnification of the first part of a).

5 Conclusions

In this thesis, different nanocomposites based on activated carbon cloth (ACC) impregnated with polymer-derived ceramics (PDCs) and subsequent pyrolysis were fabricated. The PDCs were obtained by mixing Ni-based and Co-based organometallics with a polysilazane at toluene reflux in different ratios. Along the synthesis route, the morphological and microstructural changes were studied using various methods. The suitability of the materials for their use in supercapacitors and other energy storage applications were studied by performing electrochemical measurements such as cyclic voltammetry and electrochemical impedance spectroscopy. Gas ad-/desorption measurements were carried out using N_2 at 77 K to link the electrochemical performance to the porosity properties.

The successful impregnation of ACC with PDCs using the proposed route, could be verified. However, the impregnation appeared to be very inhomogeneous which might affect the performance of the final composites. The chosen synthesis route also led to amounts of NH_4Cl in the nanocomposites that, however, could be removed by a vacuum treatment at elevated temperatures. No indication of an integration of organometallics in the matrix could be found. Furthermore, the chosen silicon-to-metal ratio hardly influenced the behaviour of the final nanocomposites. Even though all nanocomposites showed microporous behaviour, their specific surface area and total pore volume decreased compared to the pure ACC as a result of potential pore blocking with the impregnation material. The electrochemical studies indicated smaller hysteresis loops (i.e. lower energy storage capability) compared to the pure ACC. This is in accordance to the reduced specific surface area and total pore volume of the samples. Moreover, an unforeseen effect of a strong increase in capacitance with hardly any hysteresis is observed for some nanocomposites. This effect appeared especially at scanning rates of 1 mV/s and lower. This might be attributed to a decrease in conductivity of the samples. However, more detailed studies would be necessary for clarification.

The findings suggest that the produced nanocomposites are not suitable for supercapacitor applications and porosity-related applications such as hydrogen storage or water purification, as all crucial performance properties (i.e. specific surface area, total pore volume and cyclic voltammetry hysteresis) got worse compared to the pure ACC. Even though, the catalytic properties of PDCs might yield other applications for the PDC-ACC nanocomposites.

Bibliography

[1] M. C. Bechelany, V. Proust, A. Lale, P. Miele, S. Malo, C. Gervais, and S. Bernard, "Nanocomposites through the chemistry of single-source precursors: understanding the role of chemistry behind the design of monolith-type nanostructured titanium nitride/silicon nitride," *Chemistry–A European Journal*, vol. 23, no. 4, pp. 832–845, 2017.

[2] S. Komarneni, "Nanocomposites," *Journal of Materials Chemistry*, vol. 2, no. 12, pp. 1219–1230, 1992.

[3] M. Sternitzke, "Structural ceramic nanocomposites," *Journal of the European Ceramic Society*, vol. 17, no. 9, pp. 1061–1082, 1997.

[4] G. Mera, M. Gallei, S. Bernard, and E. Ionescu, "Ceramic nanocomposites from tailor-made preceramic polymers," *Nanomaterials*, vol. 5, no. 2, pp. 468–540, 2015.

[5] P. Colombo, G. Mera, R. Riedel, and G. D. Soraru, "Polymer-derived ceramics: 40 years of research and innovation in advanced ceramics," *Journal of the American Ceramic Society*, vol. 93, no. 7, pp. 1805–1837, 2010.

[6] A. Lale, M. Schmidt, M. D. Mallmann, A. V. A. Bezerra, E. D. Acosta, R. A. F. Machado, U. B. Demirci, and S. Bernard, "Polymer-derived ceramics with engineered mesoporosity: From design to application in catalysis," *Surface and Coatings Technology*, vol. 350, pp. 569–586, 2018.

[7] B. Gilland, "World population, economic growth, and energy demand, 1990-2100: a review of projections," *Population and Development Review*, pp. 507–539, 1995.

[8] G. Petrecca, "World energy demand," in *Energy Conversion and Management*, pp. 25–29, Springer, 2014.

[9] A. P. Mathews, "Renewable energy technologies: panacea for world energy security and climate change?," *Procedia Computer Science*, vol. 32, pp. 731–737, 2014.

[10] J. Libich, J. Máca, J. Vondrák, O. Čech, and M. Sedlaříková, "Supercapacitors: Properties and applications," *Journal of Energy Storage*, vol. 17, pp. 224–227, 2018.

[11] C. Koczwara, *Performance evaluation and in situ X-ray scattering of ordered meso-porous carbons for electrochemical energy storage applications*. PhD thesis, Montanuniversität Leoben, Austria, 2019.

[12] P. Simon and Y. Gogotsi, "Materials for electrochemical capacitors," in *Nanoscience and technology: a collection of reviews from Nature journals*, pp. 320–329, World Scientific, 2010.

[13] N. Natter, N. Kostoglou, C. Koczwara, C. Tampaxis, T. Steriotis, R. Gupta, O. Paris, C. Rebholz, and C. Mitterer, "Plasma-derived graphene-based materials for water purification and energy storage," *C—Journal of Carbon Research*, vol. 5, no. 2, p. 16, 2019.

[14] F. Çeçen and Ö. Aktas, *Activated carbon for water and wastewater treatment: integration of adsorption and biological treatment*. John Wiley & Sons, 2011.

[15] J. Ren, N. M. Musyoka, H. W. Langmi, M. Mathe, and S. Liao, "Current research trends and perspectives on materials-based hydrogen storage solutions: a critical review," *International Journal of Hydrogen Energy*, vol. 42, no. 1, pp. 289–311, 2017.

[16] J. M. Sieben, E. Morallon, and D. Cazorla-Amorós, "Flexible ruthenium oxide-activated carbon cloth composites prepared by simple electrodeposition methods," *Energy*, vol. 58, pp. 519–526, 2013.

[17] N. Kostoglou, C. Koczwara, C. Prehal, V. Terziyska, B. Babic, B. Matovic, G. Constantinides, C. Tampaxis, G. Charalambopoulou, T. Steriotis, *et al.*, "Nanoporous activated carbon cloth as a versatile material for hydrogen adsorption, selective gas separation and electrochemical energy storage," *Nano Energy*, vol. 40, pp. 49–64, 2017.

[18] E. Ayranci and N. Hoda, "Adsorption kinetics and isotherms of pesticides onto activated carbon-cloth," *Chemosphere*, vol. 60, no. 11, pp. 1600–1607, 2005.

[19] S. Jiang, T. Shi, X. Zhan, H. Long, S. Xi, H. Hu, and Z. Tang, "High-performance all-solid-state flexible supercapacitors based on two-step activated carbon cloth," *Journal of Power Sources*, vol. 272, pp. 16–23, 2014.

[20] H.-J. Oh, J.-H. Lee, H.-J. Ahn, Y. Jeong, Y.-J. Kim, and C.-S. Chi, "Nanoporous activated carbon cloth for capacitive deionization of aqueous solution," *Thin Solid Films*, vol. 515, no. 1, pp. 220–225, 2006.

[21] D. Gudarzi, W. Ratchananusorn, I. Turunen, M. Heinonen, and T. Salmi, "Promotional effects of au in pd–au bimetallic catalysts supported on activated carbon

cloth (acc) for direct synthesis of h2o2 from h2 and o2," *Catalysis Today*, vol. 248, pp. 58–68, 2015.

[22] I. I. Misnon, N. K. M. Zain, and R. Jose, "Conversion of oil palm kernel shell biomass to activated carbon for supercapacitor electrode application," *Waste and Biomass Valorization*, vol. 10, no. 6, pp. 1731–1740, 2019.

[23] C. Abbey and G. Joos, "Supercapacitor energy storage for wind energy applications," *IEEE transactions on Industry applications*, vol. 43, no. 3, pp. 769–776, 2007.

[24] T. A. Centeno, O. Sereda, and F. Stoeckli, "Capacitance in carbon pores of 0.7 to 15 nm: a regular pattern," *Physical Chemistry Chemical Physics*, vol. 13, no. 27, pp. 12403–12406, 2011.

[25] S. Vaquero, R. Díaz, M. Anderson, J. Palma, and R. Marcilla, "Insights into the influence of pore size distribution and surface functionalities in the behaviour of carbon supercapacitors," *Electrochimica acta*, vol. 86, pp. 241–247, 2012.

[26] J. Huang, B. G. Sumpter, and V. Meunier, "Theoretical model for nanoporous carbon supercapacitors," *Angewandte Chemie*, vol. 120, no. 3, pp. 530–534, 2008.

[27] X. Wei, X. Jiang, J. Wei, and S. Gao, "Functional groups and pore size distribution do matter to hierarchically porous carbons as high-rate-performance supercapacitors," *Chemistry of Materials*, vol. 28, no. 2, pp. 445–458, 2016.

[28] G. Wang, L. Zhang, and J. Zhang, "A review of electrode materials for electrochemical supercapacitors," *Chemical Society Reviews*, vol. 41, no. 2, pp. 797–828, 2012.

[29] C. Largeot, C. Portet, J. Chmiola, P.-L. Taberna, Y. Gogotsi, and P. Simon, "Relation between the ion size and pore size for an electric double-layer capacitor," *Journal of the American Chemical Society*, vol. 130, no. 9, pp. 2730–2731, 2008.

[30] Y. Zhang, H. Feng, X. Wu, L. Wang, A. Zhang, T. Xia, H. Dong, X. Li, and L. Zhang, "Progress of electrochemical capacitor electrode materials: A review," *International journal of hydrogen energy*, vol. 34, no. 11, pp. 4889–4899, 2009.

[31] G. Wang, H. Wang, X. Lu, Y. Ling, M. Yu, T. Zhai, Y. Tong, and Y. Li, "Solid-state supercapacitor based on activated carbon cloths exhibits excellent rate capability," *Advanced materials*, vol. 26, no. 17, pp. 2676–2682, 2014.

[32] J. Li, Y. Wang, W. Xu, Y. Wang, B. Zhang, S. Luo, X. Zhou, C. Zhang, X. Gu, and C. Hu, "Porous fe2o3 nanospheres anchored on activated carbon cloth for high-performance symmetric supercapacitors," *Nano Energy*, vol. 57, pp. 379–387, 2019.

[33] X. Zhou, Q. Chen, A. Wang, J. Xu, S. Wu, and J. Shen, "Bamboo-like composites of v2o5/polyindole and activated carbon cloth as electrodes for all-solid-state flexible asymmetric supercapacitors," *ACS applied materials & interfaces*, vol. 8, no. 6, pp. 3776–3783, 2016.

[34] Z. Lin, E. Goikolea, A. Balducci, K. Naoi, P.-L. Taberna, M. Salanne, G. Yushin, and P. Simon, "Materials for supercapacitors: When li-ion battery power is not enough," *Materials today*, vol. 21, no. 4, pp. 419–436, 2018.

[35] B. Krüner, C. Odenwald, A. Quade, G. Kickelbick, and V. Presser, "Influence of nitrogen-doping for carbide-derived carbons on the supercapacitor performance in an organic electrolyte and an ionic liquid," *Batteries & Supercaps*, vol. 1, no. 4, pp. 135–148, 2018.

[36] D. K. Gosser, *Cyclic voltammetry: simulation and analysis of reaction mechanisms*, vol. 43. VCH New York, 1993.

[37] M. Lu, *Supercapacitors: materials, systems, and applications*. John Wiley & Sons, 2013.

[38] M. P. Voigt, "Adaptive current limiting for any power source with output equivalent series resistance," Aug. 24 2010. US Patent 7,782,018.

[39] K.-B. Li, D.-W. Shi, Z.-Y. Cai, G.-L. Zhang, Q.-A. Huang, D. Liu, and C.-P. Yang, "Studies on the equivalent serial resistance of carbon supercapacitor," *Electrochimica Acta*, vol. 174, pp. 596–600, 2015.

[40] B. M. Babić, S. K. Milonjić, M. Polovina, and B. Kaludierović, "Point of zero charge and intrinsic equilibrium constants of activated carbon cloth," *Carbon*, vol. 37, no. 3, pp. 477–481, 1999.

[41] C. O. Ania and F. Béguin, "Mechanism of adsorption and electrosorption of bentazone on activated carbon cloth in aqueous solutions," *Water Research*, vol. 41, no. 15, pp. 3372–3380, 2007.

[42] S. Masson, M. Gineys, S. Delpeux-Ouldriane, L. Reinert, S. Guittonneau, F. Béguin, and L. Duclaux, "Single, binary, and mixture adsorption of nine organic contaminants onto a microporous and a microporous/mesoporous activated carbon cloth," *Microporous and Mesoporous Materials*, vol. 234, pp. 24–34, 2016.

[43] N. Kostoglou, V. Tzitzios, A. G. Kontos, K. Giannakopoulos, C. Tampaxis, A. Papavasiliou, G. Charalambopoulou, T. Steriotis, Y. Li, K. Liao, *et al.*, "Synthesis of nanoporous graphene oxide adsorbents by freeze-drying or microwave radiation:

Characterization and hydrogen storage properties," *International Journal of Hydrogen Energy*, vol. 40, no. 21, pp. 6844–6852, 2015.

[44] W. Zhao, Y. Zheng, L. Cui, D. Jia, D. Wei, R. Zheng, C. Barrow, W. Yang, and J. Liu, "Mof derived ni-co-s nanosheets on electrochemically activated carbon cloth via an etching/ion exchange method for wearable hybrid supercapacitors," *Chemical Engineering Journal*, vol. 371, pp. 461–469, 2019.

[45] M.-W. Ryoo and G. Seo, "Improvement in capacitive deionization function of activated carbon cloth by titania modification," *Water Research*, vol. 37, no. 7, pp. 1527–1534, 2003.

[46] J.-P. Boudou, "Surface chemistry of a viscose-based activated carbon cloth modified by treatment with ammonia and steam," *Carbon*, vol. 41, no. 10, pp. 1955–1963, 2003.

[47] R. A. Hayes, "The modification of activated carbon cloth/by," 1988.

[48] A. Huidobro, A. Pastor, and F. Rodrıguez-Reinoso, "Preparation of activated carbon cloth from viscous rayon: Part iv. chemical activation," *Carbon*, vol. 39, no. 3, pp. 389–398, 2001.

[49] A. Peigney, C. Laurent, E. Flahaut, R. Bacsa, and A. Rousset, "Specific surface area of carbon nanotubes and bundles of carbon nanotubes," *Carbon*, vol. 39, no. 4, pp. 507–514, 2001.

[50] T. Centeno and F. Stoeckli, "The assessment of surface areas in porous carbons by two model-independent techniques, the dr equation and dft," *Carbon*, vol. 48, no. 9, pp. 2478–2486, 2010.

[51] M. Thommes, K. Kaneko, A. V. Neimark, J. P. Olivier, F. Rodriguez-Reinoso, J. Rouquerol, and K. S. Sing, "Physisorption of gases, with special reference to the evaluation of surface area and pore size distribution (iupac technical report)," *Pure and Applied Chemistry*, vol. 87, no. 9-10, pp. 1051–1069, 2015.

[52] K. Kaneko, "Determination of pore size and pore size distribution: 1. adsorbents and catalysts," *Journal of membrane science*, vol. 96, no. 1-2, pp. 59–89, 1994.

[53] C. Pelekani and V. L. Snoeyink, "Competitive adsorption between atrazine and methylene blue on activated carbon: the importance of pore size distribution," *Carbon*, vol. 38, no. 10, pp. 1423–1436, 2000.

[54] N. Kostoglou, A. Tarat, I. Walters, V. Ryzhkov, C. Tampaxis, G. Charalambopoulou, T. Steriotis, C. Mitterer, and C. Rebholz, "Few-layer graphene-like flakes

derived by plasma treatment: a potential material for hydrogen adsorption and storage," *Microporous and Mesoporous Materials*, vol. 225, pp. 482–487, 2016.

[55] B. D. Zdravkov, J. J. Čermák, M. Šefara, and J. Jank, "Pore classification in the characterization of porous materials: A perspective," *Central European journal of chemistry*, vol. 5, no. 2, pp. 385–395, 2007.

[56] N. Kostoglou, *Carbon-based nanoporous materials for hydrogen storage*. PhD thesis, Montanuniversität Leoben, Austria, 2017.

[57] C. Ö. Karacan and E. Okandan, "Assessment of energetic heterogeneity of coals for gas adsorption and its effect on mixture predictions for coalbed methane studies," *Fuel*, vol. 79, no. 15, pp. 1963–1974, 2000.

[58] L. Czepirski, M. R. Balys, and E. Komorowska-Czepirska, "Some generalization of langmuir adsorption isotherm," *Internet Journal of Chemistry*, vol. 3, no. 14, pp. 1099–8292, 2000.

[59] M. Thommes, "Physical adsorption characterization of ordered and amorphous mesoporous materials," in *Nanoporous Materials: Science and Engineering*, pp. 317–364, World Scientific, 2004.

[60] J. Villarroel-Rocha, D. Barrera, and K. Sapag, "Introducing a self-consistent test and the corresponding modification in the barrett, joyner and halenda method for pore-size determination," *Microporous and Mesoporous Materials*, vol. 200, pp. 68–78, 2014.

[61] J. Rouquerol, F. Rouquerol, P. Llewellyn, G. Maurin, and K. S. Sing, *Adsorption by powders and porous solids: principles, methodology and applications*. Academic press, 2013.

[62] A. V. Neimark, Y. Lin, P. I. Ravikovitch, and M. Thommes, "Quenched solid density functional theory and pore size analysis of micro-mesoporous carbons," *Carbon*, vol. 47, no. 7, pp. 1617–1628, 2009.

[63] M. T. Alam and A. H. Ansari, "High strength aluminium-silicon carbide composite casting," *Indian foundry Journal*, vol. 60, no. 3, pp. 25–32, 2014.

[64] M. Kawasumi, "Nanocomposites based on organic and inorganic materials and their unique properties and functions," 2019.

[65] A. Okada and A. Usuki, "Twenty years of polymer-clay nanocomposites," *Macromolecular materials and Engineering*, vol. 291, no. 12, pp. 1449–1476, 2006.

[66] H. Matsuura, "Reconfigurated tpr is needed to formulate tackier psa," *Nippon Gomu Kyokaishi/Journal of the Society of Rubber Industry, Japan*, vol. 84, no. 3, 2011.

[67] E. Ionescu, C. Linck, C. Fasel, M. Müller, H.-J. Kleebe, and R. Riedel, "Polymer-derived sioc/zro2 ceramic nanocomposites with excellent high-temperature stability," *Journal of the American Ceramic Society*, vol. 93, no. 1, pp. 241–250, 2010.

[68] G. Mera and R. Riedel, "Polymer-derived ceramics: From nanostructure to applications," *Colombo, P., Riedel, R., Sorarù, GD, Kleebe, H., Eds*, pp. 51–89, 2009.

[69] R. Riedel, G. Mera, R. Hauser, and A. Klonczynski, "Silicon-based polymer-derived ceramics: synthesis properties and applications-a review dedicated to prof. dr. fritz aldinger on the occasion of his 65th birthday," *Journal of the Ceramic Society of Japan*, vol. 114, no. 1330, pp. 425–444, 2006.

[70] C. Vakifahmetoglu, D. Zeydanli, and P. Colombo, "Porous polymer derived ceramics," *Materials Science and Engineering: R: Reports*, vol. 106, pp. 1–30, 2016.

[71] Y. Iwamoto, K. Sato, T. Kato, T. Inada, and Y. Kubo, "A hydrogen-permselective amorphous silica membrane derived from polysilazane," *Journal of the European Ceramic Society*, vol. 25, no. 2-3, pp. 257–264, 2005.

[72] M. Wilhelm, C. Soltmann, D. Koch, and G. Grathwohl, "Ceramers—functional materials for adsorption techniques," *Journal of the European Ceramic Society*, vol. 25, no. 2-3, pp. 271–276, 2005.

[73] G. Mera and E. Ionescu, "Silicon-containing preceramic polymers," *Encyclopedia of polymer science and technology*, 2002.

[74] E. Breval, M. Hammond, and C. G. Pantano, "Nanostructural characterization of silicon oxycarbide glasses and glass-ceramics," *Journal of the American Ceramic Society*, vol. 77, no. 11, pp. 3012–3018, 1994.

[75] S. Bernard and P. Miele, "Polymer-derived boron nitride: a review on the chemistry, shaping and ceramic conversion of borazine derivatives," *Materials*, vol. 7, no. 11, pp. 7436–7459, 2014.

[76] M. Hörz, A. Zern, F. Berger, J. Haug, K. Müller, F. Aldinger, and M. Weinmann, "Novel polysilazanes as precursors for silicon nitride/silicon carbide composites without "free" carbon," *Journal of the European Ceramic Society*, vol. 25, no. 2-3, pp. 99–110, 2005.

[77] X. Guo, Y. Feng, X. Lin, Y. Liu, H. Gong, and Y. Zhang, "The dielectric and microwave absorption properties of polymer-derived sicn ceramics," *Journal of the European Ceramic Society*, vol. 38, no. 4, pp. 1327–1333, 2018.

[78] N. Sakato and T. Kitagaki, "Method for shaping green body of ceramic powder and ceramic body obtained by firing same," Jan. 29 1985. US Patent 4,496,506.

[79] P. Greil, "Near net shape manufacturing of polymer derived ceramics," *Journal of the European Ceramic Society*, vol. 18, no. 13, pp. 1905–1914, 1998.

[80] S. Kokott, L. Heymann, and G. Motz, "Rheology and processability of multi-walled carbon nanotubes—abse polycarbosilazane composites," *Journal of the European Ceramic Society*, vol. 28, no. 5, pp. 1015–1021, 2008.

[81] M. Schulz, "Polymer derived ceramics in mems/nems–a review on production processes and application," *Advances in applied ceramics*, vol. 108, no. 8, pp. 454–460, 2009.

[82] C. Elschenbroich, *Organometallics*. John Wiley & Sons, 2016.

[83] J. Seitz, J. Bill, N. Egger, and F. Aldinger, "Structural investigations of si/c/n-ceramics from polysilazane precursors by nuclear magnetic resonance," *Journal of the European Ceramic Society*, vol. 16, no. 8, pp. 885–891, 1996.

[84] A. Kojima, S. Hoshii, and T. Muto, "Characteristics of polysilazane compound and its application as coating for carbon material," *Journal of materials science letters*, vol. 21, no. 10, pp. 757–760, 2002.

[85] J. D. Torrey, R. K. Bordia, C. H. Henager, Y. Blum, Y. Shin, and W. D. Samuels, "Composite polymer derived ceramic system for oxidizing environments," *Journal of materials science*, vol. 41, no. 14, pp. 4617–4622, 2006.

[86] J. Rouquerol, P. Llewellyn, and F. Rouquerol, "Is the bet equation applicable to microporous adsorbents," *Stud. Surf. Sci. Catal*, vol. 160, no. 49.10, p. 1016, 2007.

[87] J. Lee, N. Jäckel, D. Kim, M. Widmaier, S. Sathyamoorthi, P. Srimuk, C. Kim, S. Fleischmann, M. Zeiger, and V. Presser, "Porous carbon as a quasi-reference electrode in aqueous electrolytes," *Electrochimica Acta*, vol. 222, pp. 1800–1805, 2016.

[88] Z. Li, C. Lu, Z. Xia, Y. Zhou, and Z. Luo, "X-ray diffraction patterns of graphite and turbostratic carbon," *Carbon*, vol. 45, no. 8, pp. 1686–1695, 2007.

[89] H. Fujimoto, "Theoretical x-ray scattering intensity of carbons with turbostratic stacking and ab stacking structures," *Carbon*, vol. 41, no. 8, pp. 1585–1592, 2003.

[90] P. Greil and M. Seibold, "Modelling of dimensional changes during polymer-ceramic conversion for bulk component fabrication," *Journal of materials science*, vol. 27, no. 4, pp. 1053–1060, 1992.

[91] C. Vakifahmetoglu, I. Menapace, A. Hirsch, L. Biasetto, R. Hauser, R. Riedel, and P. Colombo, "Highly porous macro-and micro-cellular ceramics from a polysilazane precursor," *Ceramics International*, vol. 35, no. 8, pp. 3281–3290, 2009.

[92] H. Li, L. Zhang, L. Cheng, Y. Wang, Z. Yu, M. Huang, H. Tu, and H. Xia, "Effect of the polycarbosilane structure on its final ceramic yield," *Journal of the European Ceramic Society*, vol. 28, no. 4, pp. 887–891, 2008.

[93] R. J. Corriu, D. Leclercq, P. H. Mutin, J. M. Planeix, and A. Vioux, "Mechanism of pyrolysis of polycarbosilanes: poly (silylethylene) and poly (dimethylsilylethylene)," *Organometallics*, vol. 12, no. 2, pp. 454–462, 1993.

[94] H. Younan, L. Binghai, M. Zhiqiang, and J. Teong, "Studies and applications of standardless edx quantification method in failure analysis of wafer fabrication," in *2008 15th International Symposium on the Physical and Failure Analysis of Integrated Circuits*, pp. 1–6, IEEE, 2008.

[95] H. Hoche, D. Allebrandt, M. Bruns, R. Riedel, and C. Fasel, "Relationship of chemical and structural properties with the tribological behavior of sputtered sicn films," *Surface and Coatings Technology*, vol. 202, no. 22-23, pp. 5567–5571, 2008.

[96] E. Erdem, V. Mass, A. Gembus, A. Schulz, V. Liebau-Kunzmann, C. Fasel, R. Riedel, and R.-A. Eichel, "Defect structure in lithium-doped polymer-derived sicn ceramics characterized by raman and electron paramagnetic resonance spectroscopy," *Physical Chemistry Chemical Physics*, vol. 11, no. 27, pp. 5628–5633, 2009.

[97] E. Frank, L. M. Steudle, D. Ingildeev, J. M. Spörl, and M. R. Buchmeiser, "Carbon fibers: precursor systems, processing, structure, and properties," *Angewandte Chemie International Edition*, vol. 53, no. 21, pp. 5262–5298, 2014.

[98] G. A. Zickler, B. Smarsly, N. Gierlinger, H. Peterlik, and O. Paris, "A reconsideration of the relationship between the crystallite size la of carbons determined by x-ray diffraction and raman spectroscopy," *Carbon*, vol. 44, no. 15, pp. 3239–3246, 2006.

[99] C. Sole, N. E. Drewett, and L. J. Hardwick, "In situ raman study of lithium-ion intercalation into microcrystalline graphite," *Faraday Discussions*, vol. 172, pp. 223–237, 2014.

[100] L. Escobar-Alarcón, M. Espinosa-Pesqueira, D. Solis-Casados, J. Gonzalo, J. Solis, M. Martinez-Orts, and E. Haro-Poniatowski, "Two-dimensional carbon nanostructures obtained by laser ablation in liquid: effect of an ultrasonic field," *Applied Physics A*, vol. 124, no. 2, p. 141, 2018.

[101] L. Malard, M. A. Pimenta, G. Dresselhaus, and M. Dresselhaus, "Raman spectroscopy in graphene," *Physics reports*, vol. 473, no. 5-6, pp. 51–87, 2009.

[102] M. T. Z. Myint, S. H. Al-Harthi, and J. Dutta, "Brackish water desalination by capacitive deionization using zinc oxide micro/nanostructures grafted on activated carbon cloth electrodes," *Desalination*, vol. 344, pp. 236–242, 2014.

[103] M. P. Cal, E. Dimotakis, M. Rood, and S. M. Larson, "The effect of chemical modification of activated carbon cloth on the adsorption capacity of organics and water vapor," tech. rep., American Chemical Society, Washington, DC (United States), 1996.

[104] S. Pohlmann, B. Lobato, T. A. Centeno, and A. Balducci, "The influence of pore size and surface area of activated carbons on the performance of ionic liquid based supercapacitors," *Physical Chemistry Chemical Physics*, vol. 15, no. 40, pp. 17287–17294, 2013.

[105] S. Prabaharan, R. Vimala, and Z. Zainal, "Nanostructured mesoporous carbon as electrodes for supercapacitors," *Journal of Power Sources*, vol. 161, no. 1, pp. 730–736, 2006.

[106] Y. J. Lee, S. Park, J. G. Seo, J. R. Yoon, J. Yi, and I. K. Song, "Nano-sized metal-doped carbon aerogel for pseudo-capacitive supercapacitor," *Current Applied Physics*, vol. 11, no. 3, pp. 631–635, 2011.

[107] N. Ogihara, Y. Itou, T. Sasaki, and Y. Takeuchi, "Impedance spectroscopy characterization of porous electrodes under different electrode thickness using a symmetric cell for high-performance lithium-ion batteries," *The Journal of Physical Chemistry C*, vol. 119, no. 9, pp. 4612–4619, 2015.

[108] X. Liu, Y. Wang, L. Zhan, W. Qiao, X. Liang, and L. Ling, "Effect of oxygen-containing functional groups on the impedance behavior of activated carbon-based electric double-layer capacitors," *Journal of Solid State Electrochemistry*, vol. 15, no. 2, pp. 413–419, 2011.